ANNUAL REVIEWS

Annual Review of Materials Research

Emerging Capabilities for the High-Throughput Characterization of Structural Materials

Daniel B. Miracle,[1] Mu Li,[2] Zhaohan Zhang,[3]
Rohan Mishra,[2,3] and Katharine M. Flores[2,3]

[1] Air Force Research Laboratory, Materials and Manufacturing Directorate, Wright-Patterson Air Force Base, Dayton, Ohio 45433-7817, USA; email: daniel.miracle@afresearchlab.com

[2] Department of Mechanical Engineering and Materials Science, Washington University in St. Louis, St. Louis, Missouri 63130, USA

[3] Institute of Materials Science and Engineering, Washington University in St. Louis, St. Louis, Missouri 63130, USA

Annu. Rev. Mater. Res. 2021. 51:23.1–23.34

The *Annual Review of Materials Research* is online at matsci.annualreviews.org

https://doi.org/10.1146/annurev-matsci-080619-022100

Keywords

high-throughput computations, high-throughput experiments, materials library, additive manufacturing, tensile ductility, autonomous materials research

Abstract

Structural materials have lagged behind other classes in the use of combinatorial and high-throughput (CHT) methods for rapid screening and alloy development. The dual complexities of composition and microstructure are responsible for this, along with the need to produce bulk-like, defect-free materials libraries. This review evaluates recent progress in CHT evaluations for structural materials. High-throughput computations can augment or replace experiments and accelerate data analysis. New synthesis methods, including additive manufacturing, can rapidly produce composition gradients or arrays of discrete alloys-on-demand in bulk form, and new experimental methods have been validated for nearly all essential structural materials properties. The remaining gaps are CHT measurement of bulk tensile strength, ductility, and melting temperature and production of microstructural libraries. A search strategy designed for structural materials gains efficiency by performing two layers of evaluations before addressing microstructure, and this review closes with a future vision of the autonomous, closed-loop CHT exploration of structural materials.

1. INTRODUCTION

Materials propel societies, and the rate at which societies move forward is linked to the rate of materials advances. The mobile phone is a case in point: In just a dozen years, it has changed the way societies communicate and live, and it was made possible by a host of materials innovations. The interactive display alone includes liquid crystal display or organic light-emitting diode materials, optically transparent and electrically conductive indium-tin-oxide touchscreen materials, and Gorilla® Glass for the protective outer layer. Dozens of other smartphone functions are enabled by new materials, such as temperature-compensated crystal oscillators that improve global positioning system accuracy, dielectric piezoceramics for antennae that communicate with cell towers and wireless networks, and quartz crystal sensor materials in accelerometers, barometers, gyroscopes, hygrometers, light sensors, magnetometers, proximity sensors, and thermometers (1). Similar connections between materials advancements and societal progress are found in the transportation (nautical, rail, automotive, aeronautical, space), energy, communications, medical, and industrial sectors. The industrial age, computer age, space age, and information age are all intimately connected to materials innovations. More than simply enabling change, new materials also propel economies.

The rate of materials advances has increased dramatically in the past several decades, and combinatorial and high-throughput (CHT) methods for characterizing new materials have played a central role in this acceleration. Pioneering studies as early as 1955 (2–5) built the foundations subsequently used to screen molecular libraries in biology, chemistry, and pharmaceutical fields, and combinatorial methods were (re)introduced to materials science in 1995 (6). CHT evaluations use materials libraries with either continuous composition gradients or an array of discrete compositions (7–10) that are characterized using methods that require minimal sample preparation, can be conducted on very small sample volumes (miniaturization), can be automated, and allow many measurements to be collected simultaneously (parallelization).

A wide variety of functional materials have been developed by CHT methods (9, 10). Structural materials support a vast array of human endeavors; a casual scan of the book *Fifty Materials That Make the World* shows that roughly 70% of the materials that shape our world are primarily structural (11). It may be surprising, then, that CHT methods are essentially unused for structural materials. Microstructure is the culprit. Structural properties are extremely sensitive to both composition and microstructure, adding many orthogonal dimensions of complexity to CHT evaluations. While varying a single parameter—composition—can significantly accelerate the discovery and development of functional materials, many additional independent iterations may be needed for structural materials. As a further complication, structural properties also depend on sample size; properties measured on samples with any dimension less than about 1 μm can be very different from bulk properties. This limits the options for structural materials because CHT relies on miniaturization.

As another barrier, CHT methods often have larger errors than conventional tests and may not produce or characterize materials under actual service conditions (9). In an age in which high precision and accuracy are expected from increasingly sophisticated methods, such screening efforts are sometimes viewed with disdain by researchers and funding agencies alike. Nevertheless, screening remains an essential first step in the development of structural materials. High-entropy alloys (HEAs) and complex, concentrated alloys (CCAs) vastly increase both composition and microstructure space, adding a new imperative to develop and employ effective CHT screening methods.

Major movements in materials science support an emerging revolution in the rapid characterization of structural materials. Integrated computational materials engineering (ICME) formally adds computations to the materials characterization toolkit (12). Artificial intelligence and machine learning add new dimensions to materials exploration. New experimental methods are being reported to characterize materials, and new synthesis methods capable of making bulk materials libraries are rapidly advancing. New strategies are being proposed to address the additional layers of complexity offered by structural materials. Finally, the Materials Genome Initiative in the United States, and similar movements elsewhere, provides the initiative to connect ongoing efforts in computations, new experimental tools, and the aggressive use of digital data (13).

The purpose of this review is to introduce the emerging capabilities for CHT characterization of structural materials. The methods presented here are primarily intended for metallic and ceramic materials. Experimental and (where appropriate) computational characterization methods are described for each property. Emerging methods to produce materials libraries are described, and a strategy to address the additional layers of complexity offered by structural materials is presented. The review ends with a future vision for the closed-loop, autonomous evaluation of structural materials.

2. HIGH-THROUGHPUT CHARACTERIZATION OF STRUCTURAL MATERIALS PROPERTIES

This review is limited to properties considered most important for structural materials. Methods that are automated and can perform many operations simultaneously significantly reduce acquisition time and are much preferred. Attractive CHT methods are characterized by high spatial resolution, short acquisition time, and low to modest levels of error or uncertainty; these values are reported for each method in **Table 1**. Standard characterization techniques and computational methods that display few or none of these features are not discussed in this article.

2.1. Phase Identification, Microstructure, and Phase Equilibria

Composition and microstructure each influence structural properties. Microstructures consist of phases, which are uniquely identified by their composition and atomic structure. Phase diagrams and phase equilibria are essential tools for alloy design. CHT methods to quantify all of these features are already widely available and commonly used (**Table 1**), and so only a brief coverage of these topics is provided.

2.1.1. Composition. Modern energy-dispersive spectroscopy (EDS) systems have a silicon drift detector (SDD) that, when combined with other features such as split detectors and thermal field emission guns, are fully capable of meeting CHT composition measurement needs (14). EDS spatial resolution is typically ≤3 μm, and measurement times on the order of milliseconds can be achieved so that over one million compositions can be collected in less than 1 h. EDS-SDD accuracy depends sensitively on the elemental concentrations measured and the operating conditions chosen. Using appropriate standards, accuracies of ±0.1 atomic percent (at%) can be achieved for major and minor elements, and accuracies better than ±100 ppm by weight can be realized for trace elemental analyses (14). EDS-SDD systems are included with most scanning electron microscope (SEM) units, and automated beam control allows both local compositions of discrete phases and the global composition of an alloy to be measured.

Table 1 Characteristics of combinatorial and high-throughput (CHT) experimental methods to characterize structural materials

Property	CHT method	Materials library	Spatial resolution	Acquisition time/test[a]	Error or repeatability	Automated or parallelized	Availability	Improvements and issues
Composition and microstructure								
Composition	Energy-dispersive spectroscopy with Si drift detector (EDS-SDD)	Bulk	~3 µm	Milliseconds (~1 million tests/h)[b]	~0.1 at%[b]	Automated and integrated with SEM	Widely available and used	None
	X-ray fluorescence (XRF), via synchrotron beamline	Thin film[c]	~1 mm	~15 s (~5,000 tests/day)	~±3 at%	Automated, usually integrated with XRD	Limited access via national facilities[d]	Improve spatial resolution
Crystal structure	X-ray diffraction (XRD), conventional unit, including micro-XRD (µXRD)	Thin film, bulk	50–500 µm[e] ~1 mm	Minutes to hours	Not applicable (NA)	Automated acquisition, analysis requires user input	Widely available and used	Improve spatial resolution, automate phase identification
	XRD, via synchrotron beamline	Thin film, bulk	~1 mm	Seconds	NA	Automated acquisition (usually integrated with XRF), analysis requires user input	Limited access via national facilities	Automate phase identification
	Electron back-scatter diffraction (EBSD)	Thin film, bulk	<200 nm	~1 ms	NA	Automated acquisition, analysis requires user input	Widely available and used	Automate phase identification
Microstructure	Optical microscopy (OM), scanning electron microscopy (SEM) (image acquisition)	Thin film, bulk	1 µm (OM) tens of nanometers (SEM)	~1 s	NA	Automated	Widely available and used	None
	Software (image analysis)	NA	NA	NA	NA	Selected user input required	Commercially available	Automate phase identification (reduce or eliminate user input)
Phase equilibria	EDS-SDD and XRD or EBSD	Bulk	See Composition, Crystal structure	See Composition, Crystal structure[f]	See Composition	See Composition, Crystal structure	See Composition, Crystal structure	Automate phase identification
Structure-insensitive properties (depend primarily on composition)								
Melting temperature	Optical contrast	Thin film	2 mm	~4 s[g]	Not reported (NR)	Parallelized	Feasibility demonstrated	Demonstrate higher temperature capability, broader applicability
Elastic modulus	Surface acoustic wave spectroscopy	Thin film, bulk	10–15 µm	1–10 s	±0.3% (±1–7% for single-crystal elastic constants, C_{ij})	Automated acquisition, analysis requires user input	Feasibility demonstrated	Reduce or eliminate user input

(*Continued*)

Table 1 (*Continued*)

Property	CHT method	Materials library	Spatial resolution	Acquisition time/test[a]	Error or repeatability	Automated or parallelized	Availability	Improvements and issues
	Nanoindentation mapping[h]	Thin film, bulk	150 nm to 10 µm	0.17–1 s	From ±1% to ±25%	Automated	Recently available, growing acceptance	None
	Spherical nano- and microindentation[h]	Bulk	0.5–50 µm (nano) millimeters (micro)	Minutes	From ±1% to ±4%	Automated	Feasibility demonstrated	Reduce acquisition time, make commercially available
Thermal conductivity	Time-domain thermoreflectance	Bulk	2–4 µm	0.3–0.4 s	±8%	Automated	Feasibility demonstrated	Reduce to common practice
Coefficient of thermal expansion	Time-domain probe-beam deflection	Bulk	Microns	NR	As low as ±6%	Automated	Feasibility demonstrated	Reduce to common practice
Oxidation	Raman spectroscopy	Thin film, bulk	250-nm to ~1-µm diameter × 1–10-µm depth	NR	NR	NR	Widely available and used	Limited to Raman-active oxides
	Rutherford backscatter spectroscopy	Thin film, bulk	NR	NR	NR	NR	Widely available and used	Limited to ~1-µm depth
	X-ray photoelectron spectroscopy	Thin film, bulk	~200-µm diameter × ~1-nm depth	~30 s	NR	NR	Commercially available	Destructive method
	Photostimulated luminescence spectroscopy	Thin film, bulk	5-µm diameter × 5–20-µm depth	Minutes	NR	NR	Commercially available	Extend beyond Al_2O_3 detection in superalloys
	Glow-discharge optical emission spectrometry	Thin film, bulk	~10-nm (depth), 1–8-mm (diameter)	Minutes	NR	NR	Commercially available, growing acceptance	Calibration curves and sputtering rates are needed to quantify results
Structure-sensitive properties (sensitive to both composition and microstructure)								
Corrosion	Many	Thin film, bulk	Various[i]	Various[i]	Various[i]	Various[i]	Various[i]	NA
Hardness	Nanoindentation mapping[h]	Thin film, bulk	150 nm to 10 µm	0.17–1 s	From ±1% to ±37%	Automated	Commercially available, growing acceptance	None
	Spherical nano- and microindentation[h]	Bulk	0.2–20 µm (nano) ~1 mm (micro)	Minutes	From ±1% to ±4%	Automated	Feasibility demonstrated	Reduce acquisition time, make commercially available
Strength and ductility	Nanoindentation mapping[h]	Thin film, bulk	150 nm to 10 µm	0.17–1 s	From ±1% to ±25%[j]	Automated	Commercially available, growing acceptance	Tensile ductility unavailable
	Spherical nano- and microindentation[h]	Bulk	0.2–20 µm (nano) ~1 mm (micro)	Minutes	From ±1% to ±4%[j]	Automated	Feasibility demonstrated	Tensile ductility unavailable, reduce acquisition time, make commercially available

(*Continued*)

Review in Advance first posted on June 3, 2021. (Changes may still occur before final publication.)

Table 1 (*Continued*)

Property	CHT method	Materials library	Spatial resolution	Acquisition time/test[a]	Error or repeatability	Automated or parallelized	Availability	Improvements and issues
	Microtension test	Thin film, bulk	Various[k]	NR	±10–20%[l]	Generally not automated or parallel, with exceptions	Feasibility demonstrated	Simplify handling, reduce acquisition time
	Rapid alloy prototyping	Bulk	2 mm × 5 mm × 18 mm	8–13 min	10%	Some processing, machining steps parallelized	Feasibility demonstrated	None
	Small punch test[h]	Bulk	0.25–0.5 mm × ~3 mm	2–10 min	±2–6%	Neither automated nor parallelized	Feasibility demonstrated	Improve tensile ductility accuracy, automate, reduce to practice, make commercially available
Fracture toughness	Small punch test[h]	Bulk	0.25–0.5 mm × ~3 mm	2–10 min	Often NR, can be large for brittle materials	Neither automated nor parallelized	Feasibility demonstrated	Establish feasibility for brittle materials
Fatigue	Vibrating cantilever	Thin film	1 µm × 1 mm × 10–12 mm	Up to 2.5 days	NR	Neither automated nor parallelized	Feasibility demonstrated	Limited applicability to bulk materials, only for thin films deposited on a substrate
Creep	Small punch test[h]	Bulk	0.5 mm × ~4 mm	200 s to 23 days	NR	Neither automated nor parallelized	Feasibility demonstrated	Improve ability to measure time to rupture, minimum creep rate
	Levitation	Bulk	2-mm sphere	Up to 7 h	±5% error in stress exponent	Neither automated nor parallelized	Feasibility demonstrated	Requires beamline with levitation unit
	Cantilever	Bulk	5 mm × 5 mm × 40 mm	15 min to 5 h	NR but appears equivalent to uniaxial creep	Neither automated nor parallelized	Feasibility demonstrated	Automate, demonstrate at higher temperatures

[a] These values do not include time to prepare the materials library or to access facilities.

[b] These values depend very sensitively on selectable operating conditions. The values shown here are typical for major and minor constituents; acquisition times are longer and errors are smaller for impurity analyses.

[c] A thin film is one in which at least one dimension is ≤1 µm.

[d] XRF is widely used and available; the more restricted sense used here is within the context of CHT applications.

[e] For µXRD.

[f] Equilibration of a materials library requires hundreds to thousands of hours.

[g] This time accounts for the parallel nature of measurements and depends on the number of samples in the materials library and the heating and cooling rates.

[h] This technique provides more than one property and is also displayed elsewhere in this table.

[i] Many different CHT tests are used for corrosion, and the features depend on the particular test. More information is available in References 90 and 91.

[j] Errors for stress are typically not reported for hardness tests and are irrelevant for strain.

[k] Many different microtensile geometries are available with dimensions that range from submicrons to many millimeters (99, 100).

[l] Taken from error bars or range of strength values reported in References 99 and 100.

X-ray fluorescence (XRF) is also used for high-throughput composition measurement (15). A high-intensity beam such as that produced in a synchrotron generates characteristic fluorescent X-rays in a sample, which are collected using wavelength-dispersive spectroscopy or EDS methods. Typical test capabilities use thin-film ($\leq$1-μm thickness) materials libraries and have a lateral spatial resolution of ~1 mm, an accuracy of ~3 at%, and an acquisition time of about 15 s, so that up to 5,000 measurements can be made per day (16). Lab-scale XRF devices are not typically used in CHT evaluations. Due to its low spatial resolution, XRF cannot measure compositions of individual phases and is generally limited to measuring average compositions.

2.1.2. Crystal structure. X-ray diffraction (XRD) and electron backscatter diffraction (EBSD) are common CHT methods to measure crystal structure. XRD can be done using conventional sealed-tube or rotating-anode devices, micro-XRD (μXRD) units, or high-flux beamlines. The 1D diffraction detectors are susceptible to incomplete crystal structure indexing in samples with large grain sizes or crystallographic texture, often requiring additional scans to index a crystal. Area detectors can reduce collection time by simultaneous 2D scanning in reciprocal space, eliminating the need for additional scans (16–21). XRD spatial resolution is typically on the order of 1 mm, and μXRD has an optional collimator that gives a spot with a 50–500-μm diameter. Scan times for lab-scale units with a 1D detector are typically up to an hour, while μXRD units using 2D detectors have collection times of 10–30 min (21, 22). Synchrotron beamlines using 2D detectors have acquisition times that are typically tens of seconds up to a minute (16, 19), but limited facilities often require a lead time of 6–12 months between proposal and experiment.

EBSD offers major advantages over XRD and μXRD. Pattern collection times are on the order of 1 ms (23), and the spatial resolution is $\leq$200 nm over a wide range of operating conditions (24). Unlike XRD and μXRD, EBSD has sufficient spatial resolution to index individual phases within a microstructure. EBSD can be integrated with commercial SEM systems so that composition and crystal structure mapping can be done at the same time. Indexing of EBSD patterns is a major bottleneck. For EBSD, the user must suggest expected structures to initiate commercial pattern indexing algorithms. The presence of phases for which initial guesses cannot be made, along with the issues mentioned below for XRD, can significantly delay EBSD pattern indexing. For CHT studies involving hundreds or thousands of patterns, this is a major barrier and an active area of research (16). For example, computations can deconvolve a large number of multiphase XRD patterns to the minimum number of (typically single-phase) patterns needed to describe the search space, significantly reducing the amount of user input (18). Machine-learning algorithms have been developed that combine EBSD images with composition and lattice parameters to autonomously identify crystal structures with fewer user decisions (25).

Indexing XRD patterns is also a barrier. Differences in lattice constants (peak positions) and peak intensities between measurements and database entries for pure elements and ideal, stoichiometric compounds generally require manual intervention. Computational tools can automatically solve XRD patterns (26–28). The first-principles-assisted structure solution (FPASS) (29) method uses the experimental composition, density, and diffraction pattern—along with candidate space groups obtained from Rietveld refinement of the diffraction pattern—as constraints. Using a genetic algorithm and density functional theory (DFT) calculations, FPASS finds the structure that best matches the XRD pattern. This method can reproduce known crystal structures without human intervention and identify previously undetermined structures from powder diffraction patterns (26, 29). FPASS can solve the structure of line compounds with perfect ordering, but it needs to be improved to tackle structures with partial occupancy. Machine-learning models, such as AgileFD (30), can also automatically identify constituent phases using compositional and structural information from XRF/EDS and XRD measurements (28, 31).

2.1.3. Microstructure. Image acquisition is fast in both optical microscope and SEM platforms, but classifying and quantifying microstructures requires substantial human input. Commercial software packages can identify common microstructural features, such as grains, phases, precipitates, and defects. Standard analyses of area fractions and grain size distributions are available, and phases can be distinguished based on morphology and validated with chemical information. These commercial tools might be adequate to support some CHT microstructure evaluations. Nevertheless, these software packages still require user input and supervision, and since the ability to generate microstructural data sets far exceeds the ability to analyze them, even a small amount of user input could become a large task in CHT analyses. Statistical modeling–based approaches for microstructure quantification and classification are becoming popular (32–34). While the microstructure of heterogeneous materials can be represented exactly with n-point spatial correlations (also called n-point statistics), it becomes computationally intractable for $n \geq 3$ (35). Two-point statistics are usually adopted in practice. For instance, two-point spatial correlations were used to identify primary alpha particles and secondary alpha colonies in α–β Ti-based alloys with 95% accuracy (36). Recently, image texture recognition was employed to develop the set of visual features that can capture the defining characteristics of individual microstructures without human input (34). A support vector machine trained with visual features could classify images into one of seven groups automatically with accuracy greater than 80%. Convolutional neural networks (CNNs) can also assist with microstructure recognition (33, 37). Nearly 1,000 scanning electron micrographs of ultrahigh carbon steel were labeled with their primary microstructure constituents, and then a combined approach using CNNs and support vector machines classified their microstructure with accuracy higher than 95% (33). Such data-driven microstructure analysis can be extended to CHT characterization given enough training data.

2.1.4. Phase equilibria. The standard experimental approach to determine phase equilibria can take up to a year. There is no shortcut to equilibration; annealing times become exponentially longer the farther the temperature is from the melting temperature, T_m. Exposures on the order of hundreds of hours are common near T_m, and anneals can last thousands of hours (several months) near $T_m/2$. Nevertheless, significant acceleration can be achieved in synthesis and characterization. Materials libraries, discussed later, synthesize many or all of the desired compositions in a single, automated process. Additive manufacturing (AM) (38–41), vapor deposition of thick layers (42, 43), and friction stir processing (FSP) (44) have all been used to produce materials libraries for phase equilibria studies, but diffusion multiples have the advantage of combining material synthesis and an equilibration anneal in the same step (45). Further, a single diffusion multiple set can have many diffusion couples and triples. For example, as many as 10 diffusion triples have been contained in a single library (46, 47). The dual-anneal diffusion multiple (DADM) approach provides phase diagram data at intermediate temperatures by adding a second annealing treatment at a lower temperature (47–49). The initial, high-temperature anneal bonds the samples and produces the composition gradient, and the lower-temperature anneal produces equilibrium phases at the lower temperature. The time to collect phase equilibria data is accelerated using CHT phase identification methods described above for composition and crystal structure.

Computationally predicted phase diagrams have revolutionized alloy design. The Calculation of Phase Diagram (CALPHAD) framework (50, 51) predicts phase equilibria based on thermodynamic functions derived from experimental data that include phase formation enthalpies and phase equilibria. Predictions are most reliable in compositional regions where large data sets exist, for example, near commercial alloy families, and reliability decreases with increasing extrapolation away from such spaces. To fill gaps in experimental data, CALPHAD models are augmented with thermodynamic parameters from materials databases, such as The Materials Project, the Open

Quantum Materials Database (OQMD), Automatic Flow for Materials Discovery (AFLOW), and Novel Materials Discovery (52, 53). For example, high-throughput DFT calculations of binary or ternary disordered alloys can be performed using small, special, quasirandom structures (54) or by explicit enumeration of all possible symmetry-unique ordered configurations within small supercells (55). These DFT energies can be combined with a cluster expansion model to predict phase stabilities of alloys with four or more principal elements, accelerating the search for quaternary and quinary solid solution alloys (56).

2.2. Structure-Insensitive Properties

Structure-insensitive properties depend primarily on alloy composition and not so strongly on microstructure. Screening of materials based on structure-insensitive properties is accelerated since the influence of microstructure is marginal. The characteristics of these CHT tests are shown in **Table 1**.

2.2.1. Melting temperature. Melting temperature is an essential property for structural materials; it influences primary and secondary processing, and most properties scale with T_m. Local melting is easily achieved via lasers, but an accurate, spatially resolved, high-throughput method to measure T_m is currently unavailable. Local temperature can be measured with optical pyrometry, but calibration for surface emissivity is required for each composition (57). Other approaches to measure T_m have been demonstrated and may also prove to have utility. For example, an entire materials library was heated in a furnace, and phase transformations (including melting) were determined by changes in optical contrast as a function of the furnace temperature (58). This approach avoids the need for calibration and for making individual temperature measurements (they are all equal to the furnace temperature), but it may be experimentally challenging to apply at high temperatures. New research is recommended to develop the capability to measure temperature using CHT methods.

Computational methods can predict T_m for metallic, ionic, and covalent systems (59, 60), but these methods lack adequate atomic potentials and are computationally expensive, limiting their use for CHT evaluations. SLUSCHI (Solid and Liquid in Ultra Small Coexistence with Hovering Interfaces) is an automated code that uses DFT calculations to calculate T_m (61). It has an accuracy on the order of ±10% or better for metallic materials. Although computation times are on the order of days, future improvements may make this a viable CHT tool.

2.2.2. Density. There are no CHT experimental approaches to measure density, but computations can evaluate it. First-principles databases provide rapid access to the theoretical density of tens of thousands of stable and metastable phases with high accuracy. For instance, The Materials Project provides access to densities of 5,257 binary and 6,192 ternary intermetallic phases. As previously noted, these databases currently do not include disordered solid solutions, for which the density can be estimated for a given composition using Vegard's law.

2.2.3. Elastic modulus. Many CHT methods measure modulus. For reasons described later (see Section 2.3.3), tests using samples with micron or submicron dimensions are not discussed here. Recent advances in laser-induced surface acoustic wave spectroscopy (SAWS) and instrumented indentation have replaced thin-film and micropillar compression methods to measure modulus. SAWS was initially demonstrated in thin films (15) and has subsequently been extended to bulk samples (62). This method is capable of evaluating Young's modulus, elastic stiffness constants (C_{ij}), and Poisson's ratio in isotropic and anisotropic materials (63). Instrumented nanoindentation also provides a high-speed modulus mapping capability (64–66). Measurements are sensitive to surface conditions, and care is needed to minimize surface roughness and chemical effects from environmental exposure to or reaction with polishing agents (15, 64, 66). Standard procedures to calibrate frame compliance and to provide the indenter area function have been established (67). In addition to the standard Berkovich nanoindenter, data collection and analysis protocols have been established for instrumented spherical nanoindentation (68, 69) and microindentation (70). Spherical indentation has a longer acquisition time and lower spatial resolution but provides lower variability and better represents bulk properties (**Table 1**).

Spatial resolution is defined by the extent of the elastic zone under the indenter. For Berkovich indenters, good accuracy is retained at indent spacings of $10h$ (h is the indent depth) (71), and indent depths range from 15 to 1,000 nm (64, 66, 71), giving spatial resolutions from ~150 nm to ~10 μm. For spherical nano- and microindentation, the indent radius at yield is ~2–5% of the indenter radius (68, 70), and the elastic zone is ~10 times the indent radius (S.R. Kalidindi, personal communication), so the spatial resolution is on the order of the indenter radius. Indenter radii are commonly 1–100 μm for spherical nanoindentation (68) and on the order of millimeters for microindentation (70). Errors in measured moduli depend on indent depth, the number of indents collected, and proximity to features such as grain or phase boundaries. Relative errors can range from ±8% to 24% for shallow indents, for a small number of measurements (64), or for complex, multiphase microstructures (66). A much smaller error of ±0.7% has been reported for large data sets in single-phase materials with deeper indents (71). A low variability for spherical nano- and microindentation results from the larger elastic zone size and ranges from roughly ±1% to ±4%, even for small data sets (68–70). Acquisition rates for instrumented nanoindenters range from $\leq 1\ \mathrm{s}^{-1}$ to $6\ \mathrm{s}^{-1}$ (64, 66, 71). Spherical indentation is less mature, and acquisition rates are presently of the order of minutes (S.R. Kalidindi, personal communication).

First-principles databases such as The Materials Project provide the elastic moduli of nearly 2,000 inorganic compounds (72), a number that is continuously growing. Automated workflows are available to rapidly calculate the elastic constants of compounds or solid solutions with minimum user input (73). DFT-calculated elastic constants are typically within 10% of experimental measurements. Machine-learning models trained with these databases enable even faster screening of candidates over broad composition and crystal structure design spaces (74).

2.2.4. Thermal properties. Time-domain thermoreflectance (TDTR) is a CHT method to measure thermal conductivity (75, 76), and time-domain probe-beam deflection (TD-PBD), an extension of TDTR, gives the coefficient of thermal expansion (CTE) (77). Extracting the CTE from the measured signal requires the density and Young's modulus of the tested materials; however, TD-PBD can independently measure Young's modulus. The accuracy can be as good as ±6%. Calculating thermal conductivity from first principles is computationally intensive and, hence, unsuitable for CHT methods. An alternative method based on a quasiharmonic Debye approximation (78) improves the calculation efficiency, but it lacks accuracy. A three-phonon quasiharmonic approximation method (79) shows good consistency with experiments on metallic and nonmetallic compounds. Its implementation in the AFLOW framework allows automated determination of finite-temperature thermal properties with computation times of the order of hours.

2.2.5. Oxidation. CHT oxidation studies have been performed on thin (≤1 μm) (for example, see 80) and thick (~50–150 μm) (81–83) alloy films produced by sputtering and ion plasma deposition (IPD), respectively. CHT studies generally screen for α-Al_2O_3 by oxidizing at intermediate (≤700°C) (80, 84–86) or high temperatures (>1,000°C) (81–83, 87) in static (80, 82, 83, 85, 86, 88) or cyclic (81, 84, 87) conditions. A range of characterization methods have been used. Optical evaluation includes color change and the presence of spallation (80, 85). Oxide thickness has been measured by X-ray photoelectron spectroscopy depth profiling (85) and automated mechanical profilometry (80). EDS gives qualitative oxygen content in thin films (85, 86, 88), and Rutherford backscattering provides oxygen levels in the surface oxide and at a specific depth below the oxide (80). XRD (80, 84, 87), XRF (87), and Raman spectroscopy (84, 87, 88) are used to determine oxide crystal structures. These techniques are typically restricted to observations within ~1 μm of the surface, but photostimulated luminescence spectroscopy can detect α-Al_2O_3 in (Co,Ni)-based superalloys at depths up to 15–20 μm (82). It is not clear to what degree the characterization methods in these studies are automated and/or parallelized, and CHT metrics such as spatial resolution, acquisition time, and reproducibility and/or error are reported infrequently. As a result of attractive features that include high erosion rates and erosion depths, good chemical sensitivity, and easy quantification for light elements (89), the glow discharge optical emission spectrometry technique is now being adapted for CHT evaluations (A. Couet, personal communication).

2.3. Structure-Sensitive Properties

Structure-sensitive properties are strongly influenced by both composition and microstructure. Properties such as hardness, strength, ductility, fracture, creep, fatigue, and corrosion behavior clearly fit in this category.

2.3.1. Corrosion.

Corrosion is complex and includes a range of attack mechanisms that depend on the type and concentration of the electrolyte; the composition, microstructure, and defect structure of the material; physical geometry; time and temperature; and the use of protection strategies such as coatings, inhibitors, and/or anodic currents (90, 91). As a result of these complexities, many CHT methods have been devised. Libraries may display variations in the substrate composition, the electrolyte, and/or the corrosion inhibitor. Microfluidic devices simulate a range of corrosion conditions, including time-dependent changes in electrolyte concentration and oxygen content. They also allow the effluent composition to be monitored continuously and are amenable to automation. Clever characterization methods include using resistance measurements as an indicator of reduced cross sections in thin wires resulting from corrosion (92) and optical characterization of a corroded substrate (93, 94) or changes in the electrolyte (92). Due to the wide range of corrosion mechanisms and CHT methods, it is difficult to give characteristic acquisition times, spatial resolutions, and reproducibility (**Table 1**). Nevertheless, significant acceleration is achieved relative to standard tests. Exposure is usually conducted in parallel, reducing acquisition time relative to standard tests by up to two orders of magnitude.

Due to the complexity of corrosion phenomena, a unifying computational model to predict corrosion resistance is missing. Empirical corrosion models are available for limited systems. For example, the pitting resistance equivalence number (95) is derived by empirically fitting to experimental Fe–Cr–Ni alloys and is unable to predict corrosion resistance in a new compositional space. Using ICME in the development of a scientifically grounded rule to quantitatively predict corrosion resistance for a given composition is being actively pursued (96).

2.3.2. Hardness.

The indentation methods described above for modulus also provide hardness. The spatial resolution for hardness and modulus are essentially the same for Berkovich indenters (64, 71), and the spatial resolution for hardness using spherical nanoindentation and microindentation is roughly 20% of the indenter diameter (S.R. Kalidindi, personal communication) (**Table 1**). Nanoindentation hardness mapping is done at strain rates that are one to two orders of magnitude higher than normal indentation tests, increasing hardness by as much as 37% (64). Sample preparation should avoid plastic deformation, for example, from aggressive grinding and mechanical polishing. The search for improved hardness can be accelerated by combining CHT-measured values with machine learning. For example, using elemental properties as descriptors, an artificial neural network was trained with 91 experimental records (97). Hardness was predicted for five HEAs in the AlCoCrFeMnNi system, and the best one had a hardness 20% higher than known alloys with a good match between predicted and measured values.

2.3.3. Strength and ductility. Strength is the distinguishing property of structural materials. Ductility is also essential and allows strength to be used to its full advantage; with limited ductility, a material often fails prematurely. Many CHT methods to evaluate strength and ductility make major concessions; compression-loading and thin-film methods are two common compromises (see the sidebar titled Compression Tests and Thin-Film Tension: Shortcuts and Compromises). Here, we briefly discuss methods that can advance CHT evaluation of strength and ductility well beyond current capabilities by overcoming these concessions. These methods should evaluate both strength and ductility, include a dominant tensile component, and provide bulk-like properties. Tests that characterize structural properties at micron or submicron dimensions, while appropriate for basic studies and for microelectromechanical systems, are less useful for the vast majority of structural applications and are not included here. Hardness tests can provide accurate strength values (98) and can give broad indications of postyield response (68), but they do not provide tensile ductility values and are not described here.

Microtensile testing has been extensively studied (99, 100). Both strength and ductility have been measured, and the uniaxial stress state simplifies analysis. Relative to standard tests, machining is accelerated by orders of magnitude using microelectrical discharge machining (99, 101), ion-beam milling through a stencil mask (102), or deep reactive ion etching (99). Microtensile testing can provide bulk-like properties since cross-sectional dimensions can be up to several hundred microns, and lengths range from hundreds of microns to millimeters. However, sample harvesting, manipulation, and gripping can be time consuming (99, 100). One strategy to overcome this issue is to produce sample arrays that remain connected to a common structure to ease handling (102, 103) and enable robust use of automation (103). AM avoids machining and can produce microtensile samples directly. Samples are larger, with cross sections typically measuring ~1 mm × 1 mm. AM can be integrated with an automated workflow that includes sample measurement, loading,

COMPRESSION TESTS AND THIN-FILM TENSION: SHORTCUTS AND COMPROMISES

Tensile stresses are present in most structural applications, and tensile fracture often occurs before competing failure modes. Compression tests suppress tensile fracture and can artificially elevate measured ductility, especially in strong, brittle materials. Thin-film tension tests offer a different compromise. Mechanical properties depend on the size of microstructural features and the specimen. Governed by the Hall-Petch relation, strengths measured in 1-μm thin films can be two to five times higher than in bulk materials with average grain diameters of d_{grain} ~100 μm, and thin-film strengths can be further elevated by submicron grain sizes. Micron-scale or submicron dimensions in micropillar compression tests can give strengths and ductilities much higher than those of the bulk material. To overcome length-scale issues, d_{grain} should be ≥ 1 μm, and the smallest sample dimension should be $\geq 10\ d_{\text{grain}}$. Compression and thin-film tension tests require much less material and machining time compared to conventional tension tests, and compression tests are easier to run, but the compromises mentioned here seriously limit their utility. Though both methods have been used for many years, neither has enabled the much-needed combinatorial revolution for structural materials. New methods that overcome these compromises are needed.

and data reduction (103), but it cannot yet reliably produce the defect-free samples needed for tension testing. Microtensile testing is a promising area for future innovation, and aggressive use of clever engineering, automation, and parallel processes may significantly reduce the time needed to produce tensile data.

The small punch test (SPT) can evaluate a broad range of structural properties (104). A sample is clamped between an upper and a lower die, and a load is applied to a spherical punch that travels through the upper die and presses the sample into a hole in the lower die (**Figure 1**). The tested volumes are large enough to give bulk properties, typically 0.2–0.5-mm thick with a 3–4-mm diameter. In a typical SPT load-displacement curve (**Figure 1**), plastic deformation initiates locally under the punch in region I; spreads throughout the sample in region II under a mixture of bending and tensile forces; undergoes tensile membrane stretching in region III; and displays damage initiation, propagation, and fracture in region IV. Yield and ultimate strengths and tensile ductility are extracted from SPT load-displacement curves using empirical relations (105), and a more direct method is now being established using an inverse solution that minimizes the difference between experimental and finite element predictions of SPT load-displacement curves (106). Thus, the SPT is another promising method for the CHT measurement of bulk, tensile strength, and ductility. Future work is needed to strengthen the connection between SPT data and uniaxial tensile properties for a broader range of structural materials, including materials with limited tensile ductility. Efforts to automate the SPT are also suggested, which may include the use of a sheet materials library with lateral dimensions that extend up to hundreds of millimeters (104). Materials libraries roughly 30 mm on a side and 0.75-mm thick have already been extracted from bulk materials to map the properties in the different microstructural regions associated with a weldment (107).

Rapid alloy prototyping introduces automation and parallel processes to otherwise conventional methods (108). Nine different material conditions were evaluated in 35 h. This approach is appropriate for modest extensions of known alloy bases with sufficient experience to support the selection of casting conditions and sufficient ductility to support rolling or other thermomechanical processes.

To calculate the strength and ductility of a random alloy, the motion and interaction of dislocations must be modeled. Such dislocation dynamics calculations are computationally intensive, but strength alone can be calculated more quickly by considering other factors, such as precipitation hardening and solid solution hardening. A high-throughput search for strengthening precipitates for different alloy systems has been conducted using DFT calculations (109, 110). By evaluating thermodynamic stability and lattice mismatch with the host lattice, about 200,000 compounds in the OQMD were screened as precipitate candidates for face-centered cubic (FCC), body-centered cubic (BCC), and hexagonal close-packed alloys (109). A similar search for 2,224 ternary metallic systems led to the discovery of 37 promising new superalloys (109). For solid solution hardening, the Labusch model (111), which uses first-principles-computed interaction energies between solute atoms and dislocations as inputs, has been used to compute the yield strength of multicomponent alloys and shows good agreement with experimental values (112, 113). This model was combined with CALPHAD (114) to create a multiobjective optimization genetic algorithm to screen thousands of BCC HEAs for optimal stability and strength. One composition with exceptional hardness was validated experimentally. In addition, the yield strengths of nine quaternary alloys were predicted with a standard error of 13% using the Suzuki model for substitutional solid solution hardening in BCC alloys (115).

Stacking fault energy is widely used to predict deformation behavior of materials. A high-throughput workflow for calculating the generalized stacking fault energies (116) is now available. As an example, to enhance the ductility of lightweight Mg alloys, a high-throughput search for

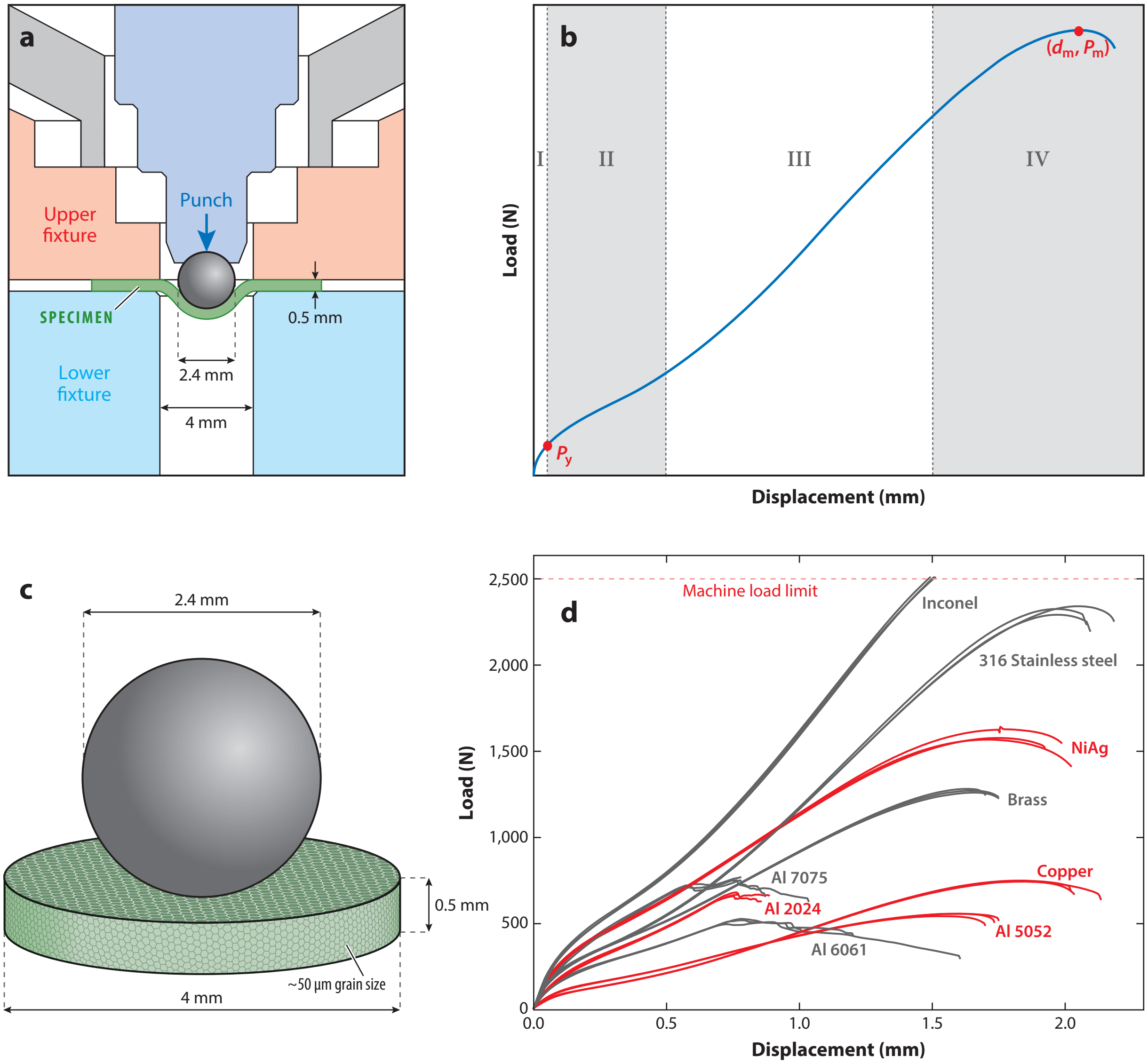

Figure 1

(*a*) Schematic of the small punch test geometry. (*b*) Illustration of a typical load-displacement curve with the four characteristic regions: (I) plastic indent and elastic stretching and yield (at P_y); (II) progressive propagation of plastic bending throughout the sample; (III) biaxial, tensile membrane stretching; and (IV) development of failure micromechanisms, necking (at the maximum displacement, d_m, and load, P_m), and final failure. (*c*) Diagram drawn to scale showing a sample and the spherical punch. To provide bulk properties, the sample thickness should be $\geq 10\ d$, where d is the average grain diameter. Sample thicknesses of 0.2–0.5 mm are commonly used. (*d*) Actual load-displacement curves for a range of metallic alloys, illustrating the clear differences in P_y, d_m, and P_m values used to determine tensile properties. Three tests were conducted for each alloy, and the high level of reproducibility is evident. The gray load-displacement curves were used as a training set, and the red curves demonstrate the predictive capability obtained via inverse solution. Panels *a*, *b*, and *d* adapted with permission from Reference 106.

Review in Advance first posted on June 3, 2021. (Changes may still occur before final publication.)

dopants (X with ∼1 at% concentration) in Mg-X alloys was performed, and 10 promising candidate elements were predicted to decrease the stacking fault energy by 25% compared to Mg. An investigation of CoCrFeNi-based FCC HEAs (117) revealed that the addition of Ti or Mo to CoCrFeNi-based HEAs increases the tendency of dislocation glide and deformation twinning during plastic deformation, and the addition of Mn, Cu, and relatively high amounts of Al promotes dislocation slip and martensitic transformation as deformation mechanisms.

2.3.4. Creep, fracture, and fatigue. Three different CHT approaches are available for creep characterization. In the first, cantilevers are subjected to a constant load by a knife-edge fixture, and a speckle pattern is deposited on one of the vertical sides to enable strain measurements with digital image correlation (DIC) (**Figure 2*a***). Stress varies with location, and strain varies with location and time; profiles of the strain along the cantilever axis, $\varepsilon_{\mathrm{xx}}$, are shown in **Figure 2*b***. Ten creep curves (five stress levels each for compression and tension) obtained at the locations indicated in **Figure 2*b*** are shown in **Figure 2*c***. The steady-state (minimum) creep rates from these 10 tests, $\dot{\varepsilon}_{ss}$, compare very well with data obtained from conventional, uniaxial tensile creep tests (**Figure 2*d***), demonstrating that the stress exponent, n, can be determined in a single CHT test (118). Test equipment and methodologies, including DIC coatings and displacement measurements, have been validated up to 750°C, and equivalence with tensile creep data has been demonstrated (119). While CHT methods often use miniaturized test volumes, recent work shows that a surface-affected region may restrict the minimum dimensions of creep samples to no less than a few millimeters (120).

The second approach uses an SPT modified for long duration tests at elevated temperatures (121). The minimum deflection rate under constant applied force and temperature in the SPT shows a good correspondence with the minimum creep rate under constant applied load in conventional creep tests (**Figure 3*a***), and a similar correspondence is seen for the time to rupture (**Figure 3*b***). Comparison of the plots in **Figure 3*b*** reveals the relationship between applied creep stress and applied SPT force, but determining the relationship between minimum creep rate and minimum SPT deflection rate remains problematic (121). The SPT also shows a good ability to reproduce trends in the Larson-Miller parameter (**Figure 3*c***), a practical method that combines the effects of stress and temperature on the time to rupture in a single plot. In the third approach, a 2-mm-diameter sphere was levitated and rotated to nearly 5,000 revolutions per second at high temperature. Strain was measured with a video camera, allowing the steady-state stress exponent, n, to be determined in a single test (122). This approach reduces the number of tests needed to determine n by nearly an order of magnitude but requires a levitation unit in line with a photon source.

Previous research has established the ability of SPT to represent fracture properties (105, 123). An approach using SPT samples with machined notches is outlined in **Figure 4*a–e***. Three analysis methods have been explored, and an approach using the area between SPT curves obtained on samples with notches of different lengths gives the best results, showing good agreement with fracture toughness measured using standard techniques on compact tension (CT) samples of 5-mm thickness (123). The time to run an SPT is not dramatically shorter than conventional fracture toughness tests. Two tests are needed to obtain a single fracture toughness value, but the machining time is likely much shorter, and the material volume is much smaller: Roughly eight SPT samples can fit inside the notch machined from a single CT sample that is 10-mm thick. Using a standard SPT sample, the fracture energy is related to the area under the load-displacement curve up to the maximum load, and a linear relation is found between the estimated biaxial fracture strain ($\varepsilon_{\mathrm{qf}}$) and fracture toughness (J_{IC}) for ductile but not for brittle materials (**Figure 4*f***) (105).

Experimental and computational advances are evident for microscale fatigue testing (for example, see 124). No work has been done on CHT fatigue testing of structural materials in bulk form.

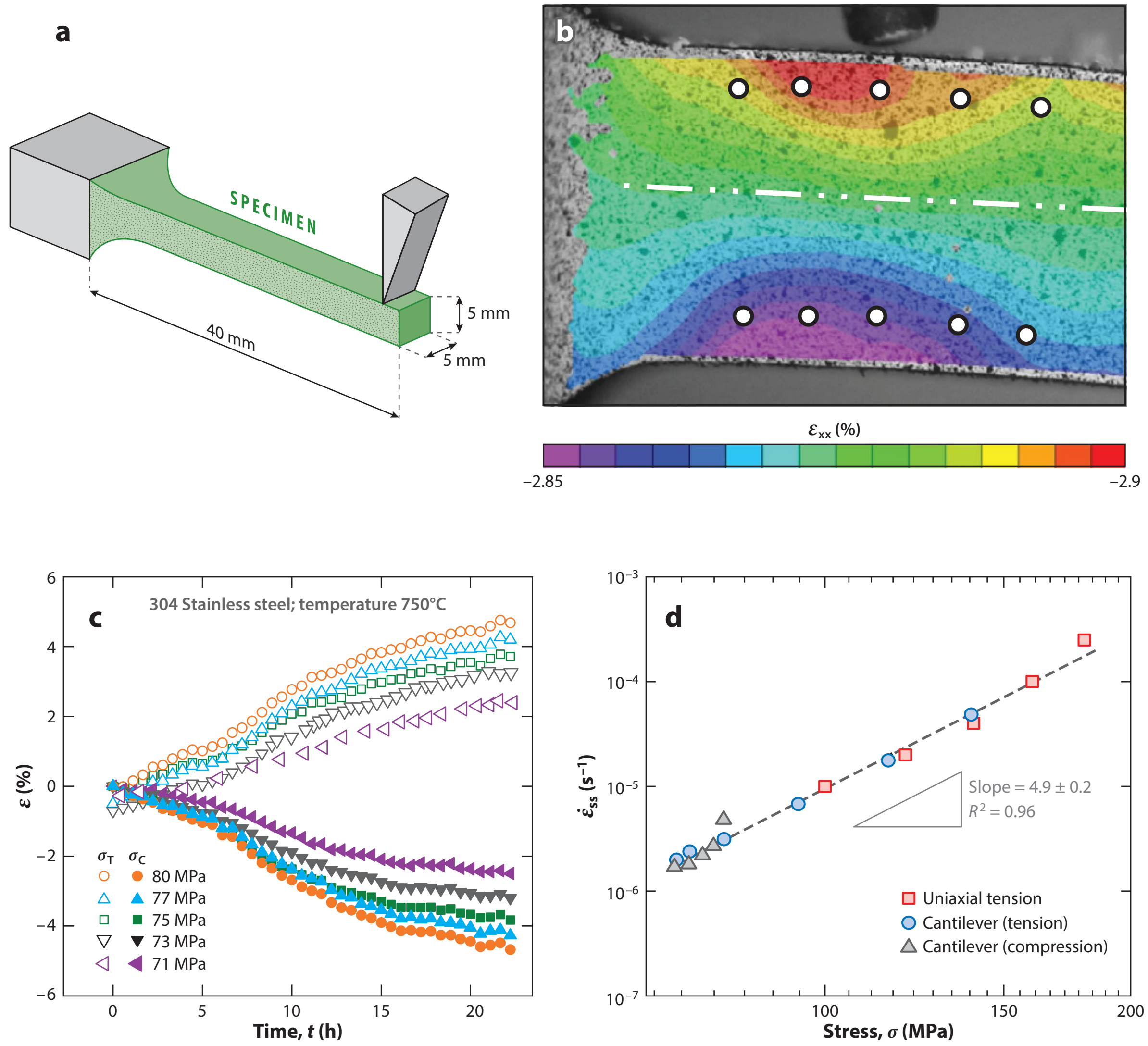

Figure 2

(*a*) Schematic of the cantilever bend creep test augmented by digital image correlation (DIC). (*b*) The speckle contrast deposited on one side of a 304 stainless steel cantilever and the superimposed axial strains after a creep test at 750°C for over 20 h. The neutral axis is indicated by the white line. (*c*) Creep curves obtained from the single sample in panel *b*, showing five representative curves for tension and five for compression taken from the points shown as open white circles in panel *b*. σ_T and σ_C are the tensile and compressive creep stresses, respectively. (*d*) Correspondence between the data obtained from curves in panel *c* with data obtained from uniaxial tensile creep tests of 304 stainless steel at 750°C. Five uniaxial tensile creep tests were required to establish the steady-state creep stress exponent, n, but only one DIC-augmented cantilever creep test was needed. Panels *b*–*d* adapted with permission from Reference 119, and the uniaxial tensile data in panel *d* are from Reference 149.

2.4. Thermomechanical Processing

Microstructure exerts a primary influence on many structural properties, and thermomechanical processing is used to control microstructure. For thermal treatments, microstructures depend on temperature and time, and heating and cooling rates are also important. Two or more

Review in Advance first posted on June 3, 2021. (Changes may still occur before final publication.)

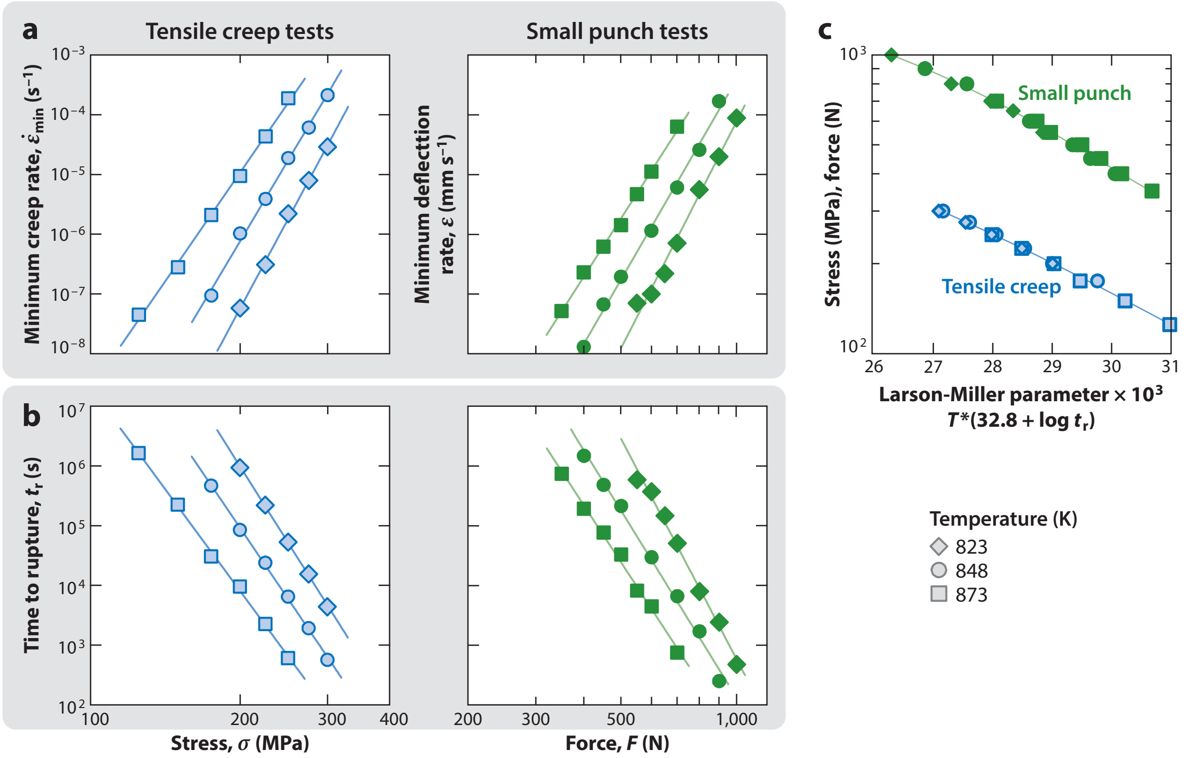

Figure 3

Comparison of the creep response of P91 chrome steel obtained via uniaxial tensile creep tests (*blue symbols*) and the small punch test (SPT) (*green symbols*). Uniaxial creep tests were performed under constant load, and SPT data were collected under constant force. Good correspondence between the two tests is shown for (*a*) minimum creep rates and (*b*) times to rupture. (*c*) Similar correspondence is shown for a Larson-Miller plot, which includes temperature, stress, and time to rupture, t_r, in a single plot. Figure adapted with permission from Reference 121.

thermal treatments can be linked together; the processes of solutionizing, quenching, and aging to produce precipitation-strengthened microstructures are well-known examples. For deformation processing, important parameters include deformation temperature, strain, and strain rate. The type of deformation matters as well; many deformation methods such as rolling, forging, and extrusion yield anisotropic strains and can produce anisotropic microstructures, and additional effort is often needed to produce isotropic microstructures. Process parameters are selected not only to give desired microstructures and shapes, but also to avoid unintended microstructural features, such as inclusions, unrecrystallized regions, crystallographic texture, or casting segregation, and to eliminate damage that can include cracks, pores, or residual stresses. Any number of thermal and mechanical treatments can be linked together, giving a vast parameter space that can be explored to produce a desired microstructure. As a result, CHT methods to rapidly design the thermomechanical processing of structural materials are expected to have a major benefit.

Methods to rapidly evaluate microstructures (see Section 2.1) and properties (see Sections 2.2 and 2.3) have been discussed. Here, we consider CHT methods to evaluate the effects of thermomechanical process parameters, such as time at temperature; heating and cooling rates; and deformation temperature, strain, and strain rate on microstructure and properties. This changes

Review in Advance first posted on
June 3, 2021. (Changes may still
occur before final publication.)

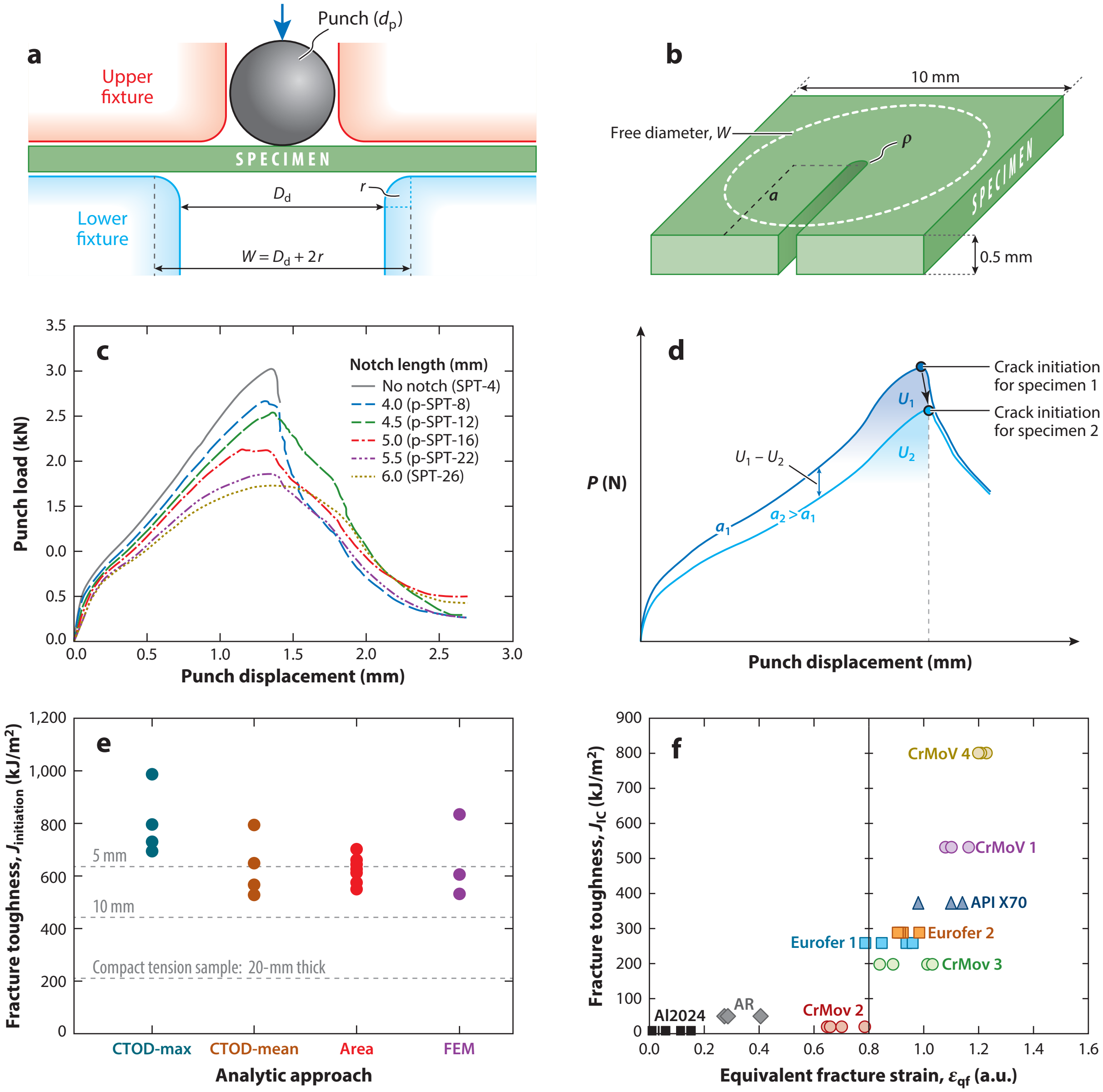

Figure 4

Correlations between fracture properties obtained by standard and combinatorial and high-throughput methods. (*a*) Schematic of an SPT loading configuration used with (*b*) a notched SPT sample. (*c*) Load-displacement curves for SPT samples with premachined notches of different lengths. (*d*) Method used to calculate the initiation fracture toughness, $J_{\text{initiation}}$, by measuring the area between two load-displacement curves with different premachined notch lengths. (*e*) Comparison of initiation fracture toughness obtained by standard methods using CT samples of 5-, 10-, and 20-mm thicknesses with values obtained by the notched SPT. The SPT values obtained using the area analysis compare well with the CT-5 standard test data. (*f*) A less rigorous comparison showing a correlation between the fracture toughness, J_{IC}, measured by standard methods for a number of steels and Al-2024 with the equivalent fracture strain, ε_{qf}, from the SPT. Abbreviations: CT, compact tension; CTOD, crack tip opening displacement; FEM, finite element method; SPT, small punch test. Panels *a*–*e* adapted with permission from Reference 123, and panel *f* adapted with permission from Reference 105.

Review in Advance first posted on June 3, 2021. (Changes may still occur before final publication.)

things around: In Sections 2.1 to 2.3, microstructure and properties were the primary outcomes of CHT evaluations, with composition as the independently controlled input. Here, composition is still independently selected, but now heat treatment and deformation parameters are also varied as inputs in the production of materials libraries, and microstructure is the measured output. The role of microstructure on mechanical properties is evaluated separately, perhaps using the same material used to establish the effect of thermomechanical variables on microstructure.

A few standard methods are currently used to establish the influence of thermomechanical process parameters through production of a microstructure gradient. The Jominy end-quench test produces a microstructure gradient by heating a standard-sized steel rod above the austenite transformation temperature and then quenching one end with a stream of water (125). The fraction of austenite that is transformed to martensite decreases with increasing distance from the quenched end. Solid samples with a controlled shape gradient have been used to produce strain gradients after fixed deformation. For example, a double-cone sample consists of a right circular disc with a truncated cone (shaped like a volcano) above and below. Upset forging of such a sample produces a radial gradient in deformation strain that can produce a graded grain size (126). Similarly, a wedge-shaped plate can be forged or rolled to a constant final thickness, producing a linear strain gradient that has been used to produce a grain size gradient (126).

Beyond these few established methods, little guidance is available for selection and design of thermomechanical processing parameters for structural materials. Earlier articles have suggested heating a material of fixed composition in a thermal gradient to produce microstructure gradients (104, 127). In the simplest form, a 1D thermal gradient can be applied to a strip or rod, producing a 1D microstructure gradient. A sheet with a composition gradient along one dimension can be placed in a furnace with a thermal gradient along the orthogonal dimension, giving information on annealing temperature and composition in a single library. A sheet of fixed composition can be used to explore the effects of a two-step thermal treatment. For example, a thermal gradient along one dimension of the sheet can explore a range of solutionizing temperatures. This sheet can be removed from the furnace, quenched, and then rotated 90° and placed in a second furnace with a thermal gradient representing a range of aging temperatures. A single sheet can then cover a wide range of both solutionizing and aging temperatures. Approaches that vary time can be imagined; for example, a series of strips could be placed in a thermal gradient and removed at different times. Similar brainstorming is needed to explore approaches to vary deformation parameters in a single library. The double-cone and wedge-shaped plate tests give total strain gradients, and analogous approaches are needed for other important deformation scenarios, including varying strain rate or varying deformation temperature. CHT methods capable of studying a wide range of important conditions have not yet been conceived and require focused thought and effort. This is an essential area for future innovation and research.

2.5. Technology Gaps and Opportunities

The previous sections illustrate a dynamic technological environment with many changes occurring simultaneously in both computational and experimental methods. This provides a fertile opportunity to conceive and develop emerging new capabilities. One such example is given here. Mechanical properties typically depend strongly on microstructure, but the critical resolved shear stress (CRSS) directly accounts for crystallographic orientation, and values are typically reported for single crystals, eliminating grain size effects. CHT methods are emerging that may enable the evaluation of the CRSS by coupling indentation methods, crystallographic orientation via EBSD, and computations providing inverse solutions, similar to the approach described for the SPT (68, 128–130). The CRSS values thus obtained could be used with crystal plasticity models to guide the exploration and characterization of additional materials. This is just one example to spark additional creative thought to establish a new CHT capability, and readers are encouraged to consider other possibilities.

3. MATERIALS LIBRARIES FOR STRUCTURAL MATERIALS

Rational design of structural materials requires data sets that link composition and microstructure to performance. However, quickly producing materials of sufficient quality to give reliable structural properties poses challenges. Accelerated synthesis methods that can be coupled with CHT property measurements are needed. CHT synthesis methods integrate controlled arrays of diverse compositions and/or microstructures into a relatively small space—an alloy library—by means of automated and parallel materials processing. In this section, we evaluate CHT synthesis approaches designed to accelerate alloy fabrication while providing reliable data for structural materials. These methods offer an additional advantage over conventional serial synthesis methods, since highly parallelized libraries eliminate uncontrolled variations in conditions during synthesis. The techniques are summarized in terms of number of samples, composition range, length scale, and compatibility with CHT characterization methods in **Table 2**.

3.1. Diffusion Multiples

A diffusion multiple involves interdiffusion between three or more blocks of different compositions that are brought into intimate mutual contact (15, 45, 47, 131). The contacting surfaces must have good surface finish (roughness of <1 μm) and be free of contamination. Hot isostatic

Table 2 Comparison of CHT synthesis methods

CHT method		Number of samples	Length scale	Required equipment	Required time	Compatible CHT characterization
Diffusion multiples		Infinite (continuous) over a complete range of constituents	Microscale	Vacuum furnace	Lengthy heat treatment (often >24 h)	SEM, EDS, EBSD, nanoindentation, oxidation
AM libraries	Bulk samples	Finite (discrete) desired compositions	Macroscale	Laser unit, inert atmosphere control, powder delivery systems, etc.	Dependent on the number, size, and height of the samples, roughly ranging from 15 min to several hours	All conventional characterization methods
	Single-layer discrete libraries	Finite (discrete) desired compositions	Submillimeter scale (thickness)			SEM, EDS, EBSD, indentation
	Continuous libraries	Infinite (continuous) over a desired composition	Microscale			SEM, EDS, EBSD, nanoindentation, oxidation
PVD libraries	Cosputtering thin films	Finite or infinite desired compositions	1–100 nm (thickness)	Evaporating power source, high vacuum chamber, sensors for precision control, etc.	Roughly ranging from 1 to 10 h, depending on thickness	SEM, EDS, EBSD, nanoindentation
	IPD and EB-DVD coatings		1–100 μm (thickness)			
Friction stir process		Infinite (continuous) over a desired composition	Microscale	Friction stir welder	Dependent on the sample size, roughly several minutes	SEM, EDS, EBSD, nanoindentation, oxidation
Rapid alloy prototyping		Finite (discrete) within the same alloy system	Macroscale	Vacuum furnace and parallel molds for serial casting	Lengthy heat treatment and thermomechanical processing (often >24 h)	All conventional characterization methods

Abbreviations: AM, additive manufacturing; CHT, combinatorial and high-throughput; EB-DVD, electron beam–directed vapor deposition; EBSD, electron backscatter diffraction; EDS, energy-dispersive spectroscopy; IPD, ion plasma deposition; PVD, physical vapor deposition; SEM, scanning electron microscope.

Review in Advance first posted on June 3, 2021. (Changes may still occur before final publication.)

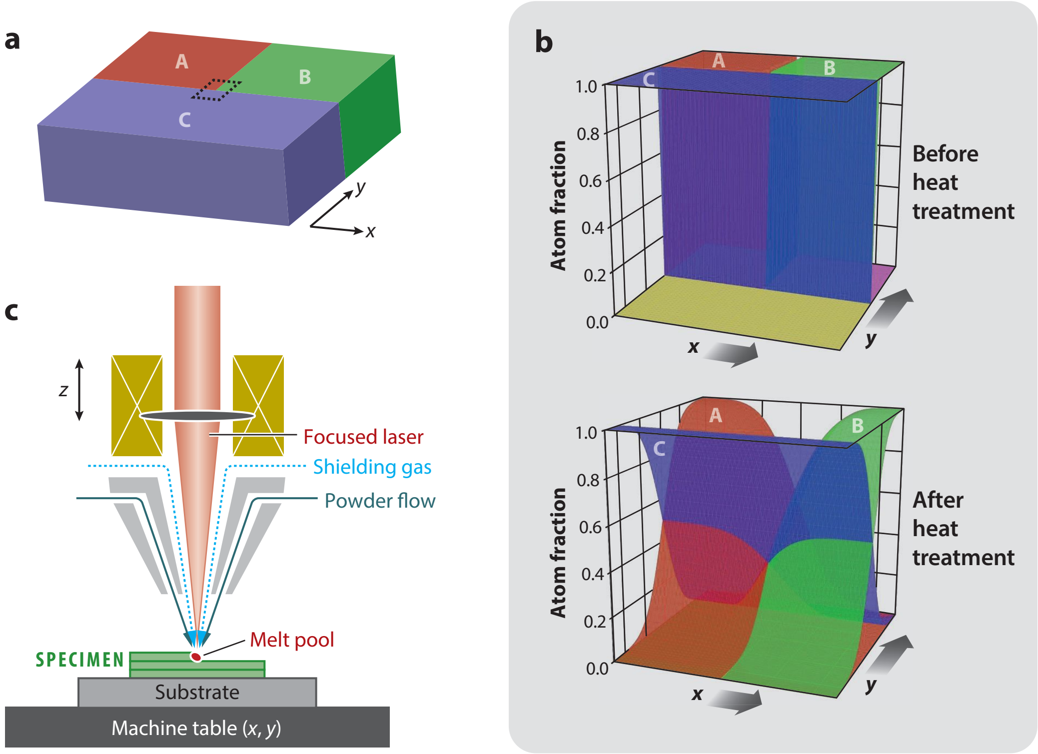

Figure 5

Two methods for producing bulk materials libraries for structural materials. (*a*) Illustration of a diffusion multiple (triple) in which A, B, and C are either single-element or prealloyed metal blocks. (*b*) Illustrations of concentration profiles before and after heat treatment. (*c*) Schematic of an additive manufacturing direct laser deposition process.

pressing provides good interface contact during bonding, followed by high-temperature annealing to achieve local equilibrium by interdiffusion. Annealing time and temperature are selected to give an interdiffusion zone of the order of ∼100 μm; this zone is small enough to minimize annealing time yet large enough to map with spatially localized characterization techniques. In a DADM, a second anneal is added to equilibrate the phases at a lower temperature (47–49). Depending on the arrangement of the blocks, diffusion couples, triples, and quadruples can be created (**Figure 5*a*,*b***), and increasing the number of blocks includes more alloy systems in a single library (46, 47). Connecting four or more blocks is rarely done due to dimensional challenges in machining needed to produce intimate mutual contact.

Diffusion multiples are especially useful for constructing phase diagrams, since the local equilibrium at the phase interfaces gives an accurate phase boundary (132, 133). This approach can also determine diffusivity (134, 135), solid solution effects and elastic modulus (136), and precipitation kinetics (45) and can map microstructures and mechanical properties with composition (133). Diffusion multiples can produce equilibrated solid solutions and intermetallic compounds over a complete range of constituent compositions thanks to the extended heat treatment at high temperature. This technique also has lower costs than other techniques. However, there are challenges. Since some phase fields transition over a scale of microns, these changes are difficult to capture; for the same reason, diffusion multiples are not compatible with measurement techniques with low spatial resolution, such as XRD and XRF. This challenge is also observed in other CHT methods that produce continuously graded libraries.

3.2. Additive Manufacturing

AM fuses metal and ceramic powder feedstock, often in complex shapes with no up-front tooling and relatively little waste. Although first used as a prototyping method, AM has drawn increasing interest as a combinatorial approach for rapid alloy development (131, 137). Two methods used for materials libraries are selective laser melting (SLM) and direct laser deposition (DLD). In SLM, a laser beam scans over a powder bed to melt and/or fuse the powder along a defined path, after which a fresh powder layer is added to the bed and the process is repeated until the desired final shape is produced. The powders may be prealloyed or consist of a blend of different powder compositions. While it is challenging to produce compositional gradients using SLM, controlling the laser parameters (power, path, travel speed) can vary the local thermal conditions and, thus, microstructural development. Due to the typically rapid heating and cooling as the laser moves, nonequilibrium microstructures are often produced.

DLD uses a laser to create a shallow melt pool on a workpiece, into which a stream of elemental, blended, or prealloyed powders is directed (**Figure 5*c***). The powders melt and are incorporated into the underlying material. Compared to SLM, DLD is more flexible for fabricating compositional libraries. Current commercial DLD systems are equipped with four or more powder reservoirs, which can mix powders in-line and transport them to the melt pool simultaneously. By independently changing the feed rate of each powder, the composition of the deposit can be changed quickly over dimensions <1 mm. Like SLM, the thermal conditions during processing can be controlled by adjusting the laser parameters, enabling both microstructure and composition control.

AM has been used to produce bulk samples of designed compositions (41, 138–140). Much of the research focuses on producing builds with homogeneous composition and defect-free microstructure. Reducing 3D build sizes to single-row thin-wall structures (141, 142) or single-layer cladding patches (40) decreases preparation time and resources but compromises the sample's amenability to certain types of CHT measurements with low spatial resolution. Libraries with controlled chemical gradients can provide a richer data set than discrete libraries (7), but the magnitude of the composition gradient needs to be considered along with the sampling size of the CHT characterization method to avoid significant composition changes within the tested volume. Such libraries are generally in a nonequilibrium state as deposited, and thermal annealing is required to provide some degree of equilibration before characterization. Libraries consisting of an array of discrete samples with individually specified compositions—alloys-on-demand—are preferred in cases where a previous evaluation step has rejected portions of the initial search space (see Section 4.1).

The sufficient mixing of powders within the melt pool is a major challenge, especially for high-melting-point elements. This challenge can be addressed by performing several remelting passes after deposition (41), but this can worsen substrate warping. It is also difficult to obtain the desired composition with elemental powders, since the flow rate and amount of each powder incorporated into the melt pool depend on powder density, size, shape, and laser absorptivity. To solve this problem, prealloyed or preblended powders are used (38), but this compromises the flexibility to produce compositionally graded libraries. The complex AM thermal history raises questions regarding the extent to which the microstructure and properties represent materials produced by conventional methods. Residual stresses and defects such as porosity, cracks, and compositional segregation are also common. Annealing is sometimes necessary to produce stable phases and mitigate defects before characterization, although this may alter intended compositional and microstructural gradients in the library. Finally, the lack of repeatability is a pervasive issue (143).

3.3. Physical Vapor Deposition Libraries

Physical vapor deposition (PVD) is a process in which the source material escapes from a target surface as a vapor phase and condenses on a substrate. Combinatorial libraries with composition gradients are produced by codeposition, the simultaneous deposition from two or more target sources. One codeposition approach sequentially deposits multiple wedge-shaped layers of continuously varying thickness from the different targets and then applies a postdeposition anneal so that the layers interdiffuse (131). Concentration gradients are produced due to the varying local thicknesses of the layers from the different targets. In the second approach, composition gradients are produced by simultaneous codeposition from two or more targets. Targets may be elemental or prealloyed compositions and are evenly spaced and confocal on the center of the substrate. Atomic-scale vapor mixtures are produced, and the local atomic fraction of each element across the substrate depends on the distance from each target to the substrate position and on deposition parameters at each target.

Sputtering produces thin films, while IPD and electron beam–directed vapor deposition (EB-DVD) produce thicker coatings. Cosputtering is a well-established industrial process and research tool and has long been used to produce CHT materials libraries (9, 131). It is adaptable to many needs, has reasonably good control over composition profiles, and produces thin films at a rate of several nanometers per minute. A vacuum arc vaporizes the target material in IPD, and the resulting high-pressure metal plasma discharges ions, atomic clusters, and nanoparticles that condense on the substrate (81). In EB-DVD, the target material is melted and vaporized by a high-voltage electron beam. IPD and EB-DVD can adopt a multitarget configuration to deposit multiple components in CHT libraries. With deposition rates ranging from 10 to 100 μm/h, thicknesses can easily exceed 100 μm, making them attractive candidates for structural materials libraries. IPD and EB-DVD have been used to investigate the effect of composition on oxidation behavior in alloys for thermal barrier coatings (42, 43, 82, 83).

There is a physical limitation in the number of targets that can be arranged around the substrate without shadowing. Multicomponent targets can increase the number of elements in the final product, although this limits the compositional range of the library. Finally, like AM libraries, rapid quenching from the vapor phase may result in nonequilibrium phases, microstructures, and defects, some of which may remain after subsequent annealing.

3.4. Other Synthesis Techniques

During FSP, a nonconsumable rotating tool is forced into a workpiece material and moved laterally, producing localized severe shear deformation and frictional heating. The combined shear stress and mass transport at high temperature produce a refined equiaxed microstructure. FSP has been used to produce composition gradients in CHT evaluations (44). Improvements are needed for further CHT application of this method. The compositional gradient can align only with the linear groove made by the tool; thus, there is only one degree of freedom in composition. Furthermore, the phases formed are metastable due to solid-state alloying. Nevertheless, this method is less capital intensive than AM or PVD and will likely have utility.

Rapid alloy prototyping, initially designed to optimize the composition of steels (108), has also been proposed as an approach for CHT synthesis of HEAs (131). This technique involves serial casting of different compositions of the same alloy system in one operation, realized by a number of parallel copper molds that can move stepwise. After each mold is filled with the molten base alloy, the composition of the melt in the furnace is precisely altered by adding a precalculated amount of alloying elements, and the next mold is filled. The batch of cast materials is hot rolled and heat treated to produce homogeneous and defect-free microstructures. This method produces bulk samples compatible with conventional characterization methods, but it can produce only a limited number of compositions at a time.

3.5. Technology Gaps and Opportunities

Compositionally graded materials libraries are ingrained in materials science thinking by many decades of use in CHT evaluations. However, structural materials also require microstructural materials libraries. A few anecdotal examples such as the Jominy bar have been used (127), but a much more expansive set of graded microstructure options are essential for progress. Postdeposition AM laser scans provide one approach (39), but the high quench rates and complex spatiothermal history of the AM process limits options. Annealing bars, strips, or sheets in furnaces with thermal gradients has also been suggested (104, 127) and is discussed in more detail in Section 2.4. The development of microstructural libraries is an area where creative thought and innovation are needed. Discrete arrays of individually specified alloy compositions are also essential. Many CHT evaluations occur after some initial screening, so the compositions that remain may not be compositionally contiguous. For example, a CALPHAD screening of over 135,000 equimolar phase diagrams identified only 34 that passed a certain set of criteria (see 144, table 14). Each of these 34 alloys contained different combinations of 13 different elements, so an alloy-on-demand library becomes the most efficient approach. AM shows great promise for this capability, but challenges need to be addressed, including the ability to have a large number of elements available for deposition.

4. A FUTURE VISION

The widespread use of any of the CHT methods described above may provide a significant advance. However, these individual capabilities can be magnified by integrating them into a synergistic CHT workflow. In this section, we give a future vision for the CHT exploration and screening of structural materials.

4.1. Strategy and Experimental Planning

A new strategy has been proposed to overcome the dual challenges of composition and microstructure in structural materials (104). Structural materials have multiple design-critical properties, and the order in which evaluations are performed has a major influence on workflow efficiency. The first principle in this strategy is that no required property is intrinsically more important than another, so there is no implicit evaluation order or hierarchy. This challenges common practice, where mechanical properties are usually evaluated first and other required properties come later. The current approach slows progress, since an alloy composition with inadequate mechanical properties cannot be rejected until microstructure is also evaluated. The second principle is that efficiency is maximized by doing first those evaluations that can eliminate the largest number of candidates with the least amount of resources (including time). Since no required property is intrinsically more important, a failure in any required property signals a failure of the alloy. This also challenges current methods, where an inordinate effort may be invested to improve deficient properties of an alloy that excels in another property, such as strength. This standard approach makes sense when the number of options is limited, but the vast expansion of alloys via HEAs and CCAs offers a new reality: If one alloy does not show strong promise to meet all requirements in an initial screening, a vast number of other candidates remain to be explored.

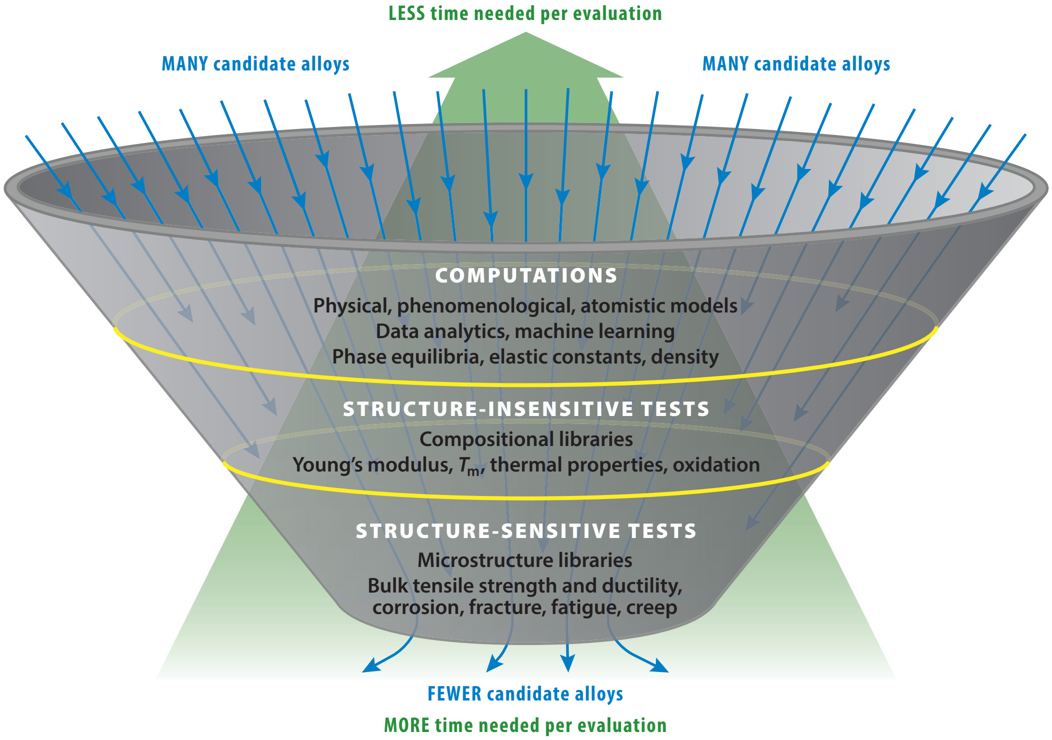

Figure 6

A strategy to accelerate the exploration and screening of structural materials. The first evaluation consists of high-throughput computations that can include physical or phenomenological models, ab initio calculations, data analytics, or machine learning. The first experimental step evaluates properties that primarily depend on composition by using materials libraries with controlled compositions (either continuous gradients or an array of distinct compositions). The final evaluation measures properties that depend sensitively on both composition and microstructure. Evaluations may be performed on materials libraries of fixed composition and controlled microstructure gradients. The resources invested in evaluating each alloy (including time) are smallest when the number of candidates is the largest and vice versa. Only alloys that pass a stage are considered in subsequent stages, motivating the need for materials libraries consisting of an array of discrete, individually specified compositions (alloys-on-demand) to skip over compositions rejected by earlier stages of this strategy.

The third principle deconstructs evaluation into three stages with a downselect at the end of each (**Figure 6**). Computational evaluations (including physical and phenomenological models, data mining, and machine learning) are done first, since they can most rapidly evaluate vast numbers of candidates with minimal resources. Structure-insensitive properties are measured next, since only composition needs to be considered. Experiments are performed on only a fraction of the initial candidates, since computations have significantly reduced the search space. As a result, materials libraries may favor discrete arrays of alloys-on-demand to skip over rejected compositions. CHT evaluations of structure-sensitive properties are done in the final stage, in which the number of candidates has been drastically reduced by the first two steps. Tests may be conducted on materials libraries of fixed composition with microstructure gradients (104, 127)

Experimental planning within this strategy considers the evaluations to be performed, the order of evaluations, definition of test conditions and pass/fail criteria, and acknowledgment of uncertainty and likelihood of false positive or negative results. It is not necessary to evaluate all required properties for an application. The order of experiments considers not only the ability to reject candidates with minimal effort, but also whether an evaluation is destructive or nondestructive. Test parameters may not match service conditions, and so setting pass/fail criteria that can accurately reflect a material's performance during service requires careful thought. Finally, experimental planning should evaluate uncertainties associated with the CHT methods and recognize the risk of false positive or negative results. An example of this experimental planning has been given for high-temperature structural metals (127).

The risk and uncertainty associated with CHT methods may cause concern, but they must be compared against a complete assessment of competing search strategies before drawing conclusions. CHT methods may have lower accuracy and higher risk, but the overall risk is significantly reduced by covering a vastly larger portion of search space. Current evaluation methods and standardized tests may provide higher accuracy and lower risk, but the overall risk is nevertheless much greater because the search space that can be evaluated is many orders of magnitude smaller. Students have a keen insight into this dilemma: In a timed test with 100 questions, is it better to be 70% certain of answers to all questions or to be 99% certain of the answer to one question?

4.2. Integrated Workflow

The envisioned future state integrates materials library synthesis with multiple CHT evaluations. This requires a materials library geometry that is common to many or all of the CHT test platforms. Current examples of an integrated workflow include those described in References 20, 40, 41, and 140. CHT methods for structural materials are still evolving, and there are no standard devices to constrain a common library geometry, so this is a good time to think holistically. The SEM is perhaps the single exception; it is used for CHT characterization of composition, crystal structure, and microstructure, so SEM chamber sizes should be considered in designing a materials library geometry. Examples of multistation, multimodal automated workflows have already been developed (145). In one, a robotic arm transports samples via a specially designed kinematic holder between characterization stations that include automated optical microscopy (Robo-Met.3D®) and an SEM with composition and EBSD mapping capabilities. The Alinstante platform builds on this concept with a robotic arm and adjacent workstations that are designed to be modular, expandable, and reconfigurable. Designing the CHT workflow for maximum efficiency may present challenges; for example, the high sample tilt required for EBSD has inspired a unique materials library configuration (140). Further, it may be desirable to remove individual samples from a library for some CHT evaluations, such as strength and ductility via SPT. To address these challenges, the materials library may be designed to break into smaller segments or to enable removal of individual samples.

4.3. Autonomous, Closed-Loop Iteration

The final component of this future vision links the first two through autonomous, closed-loop iteration. The current CHT workflow is relatively static, and the opportunity to apply new information occurs infrequently—after data analysis of iteration I and before experimental planning of iteration $I + 1$. All samples in each iteration are synthesized, characterized, and analyzed based on the knowledge available at the experimental planning phase. In the envisioned future state, an iteration may consist of a smaller number of samples or perhaps a single sample. The sample(s) in this reduced library is synthesized and characterized, and the new data update the knowledge base and devise the next iteration. The larger number of iterations accelerates learning by updating models and knowledge more frequently. As an essential feature, the workflow is done in an autonomous, closed-loop fashion using unsupervised machine learning. Such closed-loop, autonomous operation has already been demonstrated (146), and increased iterations through

Bayesian learning have reduced the number of experiments by a factor of 60 (147). While a great step forward, existing demonstrations have been limited to materials that can be synthesized on the fly, such as polymers and carbon nanotubes. With emerging synthesis capabilities such as AM, autonomous, closed-loop iteration is now conceivable for bulk metallic and ceramic structural materials. Further, existing validations focus on a single objective function, such as carbon nanotube growth rate (146) or structural toughness (147). The vision here is to build the capability to explore and screen structural materials against multiple objective functions. This is a challenging, long-term vision that requires focused research on a number of topics, including materials synthesis, CHT experimentation, models linking composition and microstructure to properties, and unsupervised machine learning algorithms capable of optimizing across multiple (and sometimes competing) objective functions and of recommending subsequent, high-value alloys and experiments. This vision has been captured by the compelling question, "What if we were able to have a Moore's law for the speed of research?" (148).

SUMMARY POINTS

1. Combinatorial and high-throughput (CHT) evaluation of structural materials lags behind other fields due to the dual constraints of composition and microstructure, as well as the strong influence of sample and microstructure length scales on many structural properties. Samples and microstructures with a minimum dimension on the order of ∼1 μm or less have limited ability to represent many important bulk structural properties.
2. Bulk-like materials libraries are needed to overcome issues associated with submicron-sample or microstructure dimensions. Additive manufacturing (AM) is an enabling technology that can rapidly make bulk materials libraries as continuous composition gradients or as an array of discrete alloys-on-demand. However, processing defects currently render AM materials inadequate for many mechanical properties, and eliminating these defects is a major area of research. Diffusion multiple libraries are especially well suited for phase equilibria studies and also provide a platform for other CHT evaluations. New approaches for producing materials libraries with fixed composition but controlled microstructure gradients are needed not only to explore the influence of microstructure on properties, but also to rapidly evaluate and establish candidate thermomechanical processes needed to produce new structural alloys.
3. High-throughput computations are an integral part of the CHT workflow. These computations are an important first step because they evaluate some properties more quickly than can be done experimentally, with adequate accuracy, and they are the only method to rapidly evaluate properties such as density. Computations are also coupled with experiments, extending capabilities and providing new synergies. Computations can automate many aspects of data analysis, and computational methods such as unsupervised machine learning are essential for achieving the future goal of autonomous, closed-loop integration.
4. CHT measurements for composition, crystal structure, microstructure, and phase equilibria are well established and are already integrated into scanning electron microscopes. Feasibility has been demonstrated for CHT measurements of nearly all essential structure-insensitive and structure-sensitive properties, but work is still

required to improve spatial resolution and accuracy and to reduce acquisition time. The small punch test seems particularly adaptable and has been used to measure tensile, creep, and fracture properties. The largest future impact is expected for establishing and reducing to practice CHT measurements for tensile strength and ductility of bulk materials. Microtensile testing and the small punch test are promising candidates. CHT measurement of melting temperature is another important need.

5. A CHT strategy for structural materials accelerates the workflow by specifying the order in which evaluations are performed. Evaluations (usually computations) that can reject the largest number of candidates with the least amount of resources (including time) are done first; structure-insensitive properties, which depend primarily on composition, are done next; and structure-sensitive properties are done last, as the combined influence of composition and microstructure often require the largest investment of resources. A downselect at the end of each phase reduces the number of tests performed in subsequent, more time-intensive evaluations.
6. A future vision looks beyond simply reducing the number of tests to practicing individual CHT methods and acknowledges a growing trend to intentionally design a materials library platform that maximizes compatibility with subsequent evaluation platforms. This vision further recognizes advancements in other disciplines that can enable autonomous, closed-loop integration of the CHT workflow. This is a grand challenge for the future.

DISCLOSURE STATEMENT

The authors are not aware of any affiliations, memberships, funding, or financial holdings that might be perceived as affecting the objectivity of this review.

ACKNOWLEDGMENTS

The authors appreciate the insights and experience shared freely by many colleagues, including Adrien Couet, Kevin Hemker, Vikram Jayaram, Surya Kalidindi, Sebastian Kube, Nicolas Leclerc, Benji Maruyama, Tresa Pollock, Dan Thoma, Mike Uchic, Ken Vecchio, and J.-C. Zhao. K.M.F. and R.M. acknowledge the National Science Foundation for support through grant DMR-1809571. D.M. acknowledges support from the Materials and Manufacturing Directorate of the Air Force Research Laboratory.

LITERATURE CITED

1. Gocha A. 2018. Smart materials make smartphones. *Am. Ceram. Soc. Bull.* 97:11–23
2. Boettcher A, Haase G, Thun R. 1955. Structural investigation of multicomponent systems by kinematic electron diffraction. *Z. Metallkd.* 46:386–400
3. Kennedy K, Stefansky T, Davy G, Zackay VF, Parker ER. 1965. Rapid method for determining ternary-alloy phase diagrams. *J. Appl. Phys.* 36:3808–10
4. Hanak JJ. 1970. The “multiple-sample concept” in materials research: synthesis, compositional analysis and testing of entire multicomponent systems. *J. Mater. Sci.* 5:964–71
5. Hanak JJ. 1971. Compositional determination of rf Co-sputtered multicomponent systems. *J. Vac. Sci. Technol.* 8:172–75
6. Xiang X-D, Sun X, Briceño G, Lou Y, Wang K-A, et al. 1995. A combinatorial approach to materials discovery. *Science* 268:1738–40

7. Rajan K. 2008. Combinatorial materials sciences: experimental strategies for accelerated knowledge discovery. *Annu. Rev. Mater. Res.* 38:299–322
8. Potyrailo R, Rajan K, Stoewe K, Takeuchi I, Chisholm B, Lam H. 2011. Combinatorial and high-throughput screening of materials libraries: review of state of the art. *ACS Comb. Sci.* 13:579–633
9. Green M, Takeuchi I, Hattrick-Simpers JR. 2013. Applications of high throughput (combinatorial) methodologies to electronic, magnetic, optical, and energy-related materials. *J. Appl. Phys.* 113:231101
10. Green ML, Choi CL, Hattrick-Simpers JR, Joshi AM, Takeuchi I, et al. 2017. Fulfilling the promise of the materials genome initiative with high-throughput experimental methodologies. *Appl. Phys. Rev.* 4:011105
11. Baker I. 2018. *Fifty Materials That Make the World*. Cham, Switz.: Springer Int. Publ.
12. Natl. Res. Counc. Comm. Integr. Comput. Mater. Eng. 2008. *Integrated Computational Materials Engineering: A Transformational Discipline for Improved Competitiveness and National Security*. Washington, DC: Natl. Acad. Press
13. Natl. Sci. Technol. Counc. 2011. *Materials Genome Initiative for Global Competitiveness*. Washington, DC: Executive Off. Pres.
14. Newbury DE, Ritchie NWM. 2013. Elemental mapping of microstructures by scanning electron microscopy-energy dispersive X-ray spectrometry (SEM-EDS): extraordinary advances with the silicon drift detector (SDD). *J. Anal. At. Spectrom.* 28:973–88
15. Zhao J-C. 2006. Combinatorial approaches as effective tools in the study of phase diagrams and composition–structure–property relationships. *Prog. Mat. Sci.* 51:557–631
16. Gregoire JM, Van Campen DG, Miller CE, Jones RJR, Surama SK, Mehta A. 2014. High-throughput synchrotron X-ray diffraction for combinatorial phase mapping. *J. Synchrotron Radiat.* 21:1262–68
17. Flemming RL. 2007. Micro X-ray diffraction (μXRD): a versatile technique for characterization of Earth and planetary materials. *Can. J. Earth Sci.* 44:1333–46
18. Long CJ, Bunker D, Li X, Karen VL, Takeuchi I. 2009. Rapid identification of structural phases in combinatorial thin-film libraries using x-ray diffraction and non-negative matrix factorization. *Rev. Sci. Instrum.* 80:103902
19. Ren F, Pandolfi R, Van Campen D, Hexemer A, Mehta A. 2017. On-the-fly data assessment for high-throughput X-ray diffraction measurements. *ACS Comb. Sci.* 19:377–85
20. Kube SA, Sohn S, Uhl D, Datye A, Mehta A, Schroers J. 2019. Phase selection motifs in high entropy alloys revealed through combinatorial methods: Large atomic size difference favors BCC over FCC. *Acta Mater*. 166:677–86
21. Eschen K, Garcia-Barriocanal J, Abel J. 2020. In-situ strain- and temperature-control X-ray micro-diffraction analysis of nickel–titanium knitted architectures. *Materialia* 11:100684
22. Xue J, Zhang L, Zou L, Liao Y, Li J, et al. 2008. High-resolution X-ray microdiffraction analysis of natural teeth. *J. Synchrotron Radiat.* 15:235–38
23. Kaufmann K, Zhu C, Rosengarten AS, Vecchio KS. 2020. Deep neural network enabled space group identification in EBSD. *Microsc. Microanal.* 26:447–57
24. Chen D, Kuo J-C, Wu W-T. 2011. Effect of microscopic parameters on EBSD spatial resolution. *Ultramicroscopy* 111:1488–94
25. Kaufmann K, Zhu C, Rosengarten AS, Maryanovsky D, Wang H, Vecchio KS. 2020. Phase mapping in EBSD using convolutional neural networks. *Microsc. Microanal.* 26:458–68
26. Ward L, Michel K, Wolverton C. 2017. Automated crystal structure solution from powder diffraction data: validation of the first-principles-assisted structure solution method. *Phys. Rev. Mater.* 1:063802
27. Oviedo F, Ren Z, Sun S, Settens C, Liu Z, et al. 2019. Fast and interpretable classification of small X-ray diffraction datasets using data augmentation and deep neural networks. *NPJ Comput. Mater.* 5:60
28. Lee J-W, Park WB, Lee JH, Singh SP, Sohn K-S. 2020. A deep-learning technique for phase identification in multiphase inorganic compounds using synthetic XRD powder patterns. *Nat. Commun.* 11:86
29. Meredig B, Wolverton C. 2013. A hybrid computational–experimental approach for automated crystal structure solution. *Nat. Mater.* 12:123–27
30. Suram SK, Xue Y, Bai J, Le Bras R, Rappazzo B, et al. 2017. Automated phase mapping with AgileFD and its application to light absorber discovery in the V–Mn–Nb oxide system. *ACS Comb. Sci.* 19:37–46

31. Baumes LA, Moliner M, Corma A. 2009. Design of a full-profile-matching solution for high-throughput analysis of multiphase samples through powder X-ray diffraction. *Chem. Eur. J.* 15:4258–69
32. Chowdhury A, Kautz E, Yener B, Lewis D. 2016. Image driven machine learning methods for microstructure recognition. *Comput. Mater. Sci.* 123:176–87
33. DeCost BL, Francis T, Holm EA. 2017. Exploring the microstructure manifold: image texture representations applied to ultrahigh carbon steel microstructures. *Acta Mater*. 133:30–40
34. DeCost BL, Holm EA. 2015. A computer vision approach for automated analysis and classification of microstructural image data. *Comput. Mater. Sci.* 110:126–33
35. Torquato S. 2002. *Random Heterogeneous Materials: Microstructure and Macroscopic Properties*. New York: Springer-Verlag
36. Kalidindi SR, Niezgoda SR, Salem AA. 2011. Microstructure informatics using higher-order statistics and efficient data-mining protocols. *JOM* 63:34–41
37. Azimi SM, Britz D, Engstler M, Fritz M, Mücklich F. 2018. Advanced steel microstructural classification by deep learning methods. *Sci. Rep.* 8:2128
38. Gwalani B, Soni V, Waseem OA, Mantri SA, Banerjee R. 2019. Laser additive manufacturing of compositionally graded AlCrFeMoV$_x$ ($x = 0$ to 1) high-entropy alloy system. *Opt. Laser Technol.* 113:330–37
39. Li M, Flores KM. 2020. Laser processing as a high-throughput method to investigate microstructure-processing-property relationships in multiprincipal element alloys. *J. Alloys Cmpds.* 825:154025
40. Li M, Gazquez J, Borisevich A, Mishra R, Flores KM. 2018. Evaluation of microstructure and mechanical property variations in Al$_x$CoCrFeNi high entropy alloys produced by a high-throughput laser deposition method. *Intermetallics* 95:110–18
41. Moorehead M, Bertsch K, Niezgoda M, Parkin C, Elbakhshwan M, et al. 2020. High-throughput synthesis of Mo-Nb-Ta-W high-entropy alloys via additive manufacturing. *Mater. Des.* 187:108358
42. Hass DD, Dharmasena K, Wadley HNG. 2002. *An electron beam method for creating combinatorial libraries: application to next generation thermal barrier coatings systems*. Rep., Def. Tech. Inf. Cent., Fort Belvoir, VA. **https://apps.dtic.mil/sti/citations/ADA466071**
43. Yu Z, Dharmasena KP, Hass DD, Wadley HNG. 2006. Vapor deposition of platinum alloyed nickel aluminide coatings. *Surf. Coat. Technol.* 201:2326–34
44. Shukla S, Wang T, Frank M, Agrawal P, Sinha S, et al. 2020. Friction stir gradient alloying: a novel solid-state high throughput screening technique for high entropy alloys. *Mater. Today Commun.* 23:100869
45. Zhao J-C. 2005. The diffusion-multiple approach to designing alloys. *Annu. Rev. Mater. Res.* 35:51–73
46. Zhao J-C, Zheng X, Cahill DG. 2005. High-throughput diffusion multiples. *Mater. Today* 8:28–37
47. Zhao J-C. 2020. High-throughput and systematic study of phase transformations and metastability using dual-anneal diffusion multiples. *Metall. Mater. Trans. A* 51:5006–22
48. Cao S, Zhao J-C. 2015. Application of dual-anneal diffusion multiples to the effective study of phase diagrams and phase transformations in the Fe–Cr–Ni system. *Acta Mater*. 88:196–206
49. Cao S, Zhao J-C. 2016. Determination of the Fe-Cr-Mo phase diagram at intermediate temperatures using dual-anneal diffusion multiples. *J. Phase Equilib. Diffus.* 37:25–38
50. Kaufman L. 2001. Computational thermodynamics and materials design. *Calphad* 25:141–61
51. Saunders N, Miodownik AP. 1998. *CALPHAD Calculation of Phase Diagrams: A Comprehensive Guide*. Oxford, UK: Pergamon/Elsevier Sci.
52. van de Walle A, Asta M, Ceder G. 2002. The alloy theoretic automated toolkit: a user guide. *Calphad* 26:539–53
53. Bigdeli S, Zhu L-F, Glensk A, Grabowski B, Lindahl B, et al. 2019. An insight into using DFT data for Calphad modeling of solid phases in the third generation of Calphad databases, a case study for Al. *Calphad* 65:79–85
54. Zunger A, Wei S, Ferreira LG, Bernard JE. 1990. Special quasirandom structures. *Phys. Rev. Lett.* 65:353–56
55. Hart GLW, Forcade RW. 2008. Algorithm for generating derivative structures. *Phys. Rev. B* 77:224115
56. Lederer Y, Toher C, Vecchio KS, Curtarolo S. 2018. The search for high entropy alloys: a high-throughput ab-initio approach. *Acta Mater*. 159:364–83
57. Martan J, Cibulka O, Semmar N. 2006. Nanosecond pulse laser melting investigation by IR radiometry and reflection-based methods. *Appl. Surf. Sci.* 253:1170–77

58. Ding S, Gregoire J, Vlassak JJ, Schroers J. 2012. Solidification of Au-Cu-Si alloys investigated by a combinatorial approach. *J. Appl. Phys.* 111:114901
59. Mei J, Davenport JW. 1992. Free-energy calculations and the melting point of Al. *Phys. Rev. B* 46:21–25
60. Morris JR, Wang CZ, Ho KM, Chan CT. 1994. Melting line of aluminum from simulations of coexisting phases. *Phys. Rev. B* 49:3109–15
61. Hong Q-J, van de Walle A. 2016. A user guide for SLUSCHI: solid and liquid in ultra small coexistence with hovering interfaces. *Calphad* 52:88–97
62. Zhao P, Zhao J-C, Weaver R. 2013. Dynamic surface acoustic response to a thermal expansion source on an anisotropic half space. *J. Acoust. Soc. Am.* 133:2634–40
63. Du X, Zhao J-C. 2017. Facile measurement of single-crystal elastic constants from polycrystalline samples. *NPJ Comput. Mater.* 3:17
64. Hintsala ED, Hangen U, Stauffer DD. 2018. High-throughput nanoindentation for statistical and spatial property determination. *JOM* 70:494–503
65. Karimzadeh A, Koloor SSR, Ayatollahi MR, Bushroa AR, Yahya MY. 2019. Assessment of nanoindentation method in mechanical characterization of heterogeneous nanocomposite materials using experimental and computational approaches. *Sci. Rep.* 9:15763
66. Vignesh B, Oliver WC, Kumar GS, Sudharshan Phani P. 2019. Critical assessment of high speed nanoindentation mapping technique and data deconvolution on thermal barrier coatings. *Mater. Des.* 181:108084
67. Galetto M, Maculotti G, Genta G, Barbato G, Levi R. 2019. Instrumented indentation test in the nanorange: performances comparison of testing machines calibration methods. *Nanomanuf. Metrol.* 2:91–99
68. Pathak S, Kalidindi SR. 2015. Spherical nanoindentation stress–strain curves. *Mater. Sci. Eng. R* 91:1–36
69. Parvinian S, Yabansu YC, Khosravani A, Garmestani H, Kalidindi SR. 2020. High-throughput exploration of the process space in 18% Ni (350) maraging steels via spherical indentation stress–strain protocols and Gaussian process models. *Integr. Mater. Manuf. Innov.* 9:199–212
70. Weaver JS, Khosravani A, Castillo A, Kalidindi SR. 2016. High throughput exploration of process-property linkages in Al-6061 using instrumented spherical microindentation and microstructurally graded samples. *Integr. Mater. Manuf. Innov.* 5:192–211
71. Sudharshan Phani P, Oliver WC. 2019. A critical assessment of the effect of indentation spacing on the measurement of hardness and modulus using instrumented indentation testing. *Mater. Des.* 164:107563
72. de Jong M, Chen W, Angsten T, Jain A, Notestine R, et al. 2015. Charting the complete elastic properties of inorganic crystalline compounds. *Sci. Data* 2:150009
73. Liu Z. 2020. ElasTool: an automated toolkit for elastic constants calculation. arXiv:2002.06535 [physics.com-ph]
74. de Jong M, Chen W, Notestine R, Persson K, Ceder G, et al. 2016. A statistical learning framework for materials science: application to elastic moduli of k-nary inorganic polycrystalline compounds. *Sci. Rep.* 6:34256
75. Huxtable S, Cahill DG, Fauconnier V, White JO, Zhao J-C. 2004. Thermal conductivity imaging at micrometre-scale resolution for combinatorial studies of materials. *Nat. Mater.* 3:298–301
76. Zhao J-C, Zheng X, Cahill DG. 2012. Thermal conductivity mapping of the Ni–Al system and the beta-NiAl phase in the Ni–Al–Cr system. *Scr. Mater.* 66:935–38
77. Zheng X, Cahill DG, Weaver R, Zhao J-C. 2008. Micron-scale measurements of the coefficient of thermal expansion by time-domain probe beam deflection. *J. Appl. Phys.* 104:073509
78. Toher C, Plata J, Levy O, Jong M, Asta M, et al. 2014. High-throughput computational screening of thermal conductivity, Debye temperature, and Grüneisen parameter using a quasiharmonic Debye model. *Phys. Rev. B* 90:174107
79. Nath P, Usanmaz D, Hicks D, Oses C, Fornari M, et al. 2019. AFLOW-QHA3P: robust and automated method to compute thermodynamic properties of solids. *Phys. Rev. Mater.* 3:073801
80. König D, Eberling C, Kieschnick M, Virtanen S, Ludwig A. 2015. High-throughput investigation of the oxidation and phase constitution of thin-film Ni–Al–Cr materials libraries. *Adv. Eng. Mater.* 17:1365–73
81. Adharapurapu RR, Zhu J, Dheeradhada VS, Lipkin DM, Pollock TM. 2014. A combinatorial investigation of palladium and platinum additions to β-NiAl overlay coatings. *Acta Mater*. 77:379–93

82. Stewart CA, Suzuki A, Pollock TM, Levi CG. 2018. Rapid assessment of oxidation behavior in Co-based γ/γ' alloys. *Oxid. Met.* 90:485–98
83. Stewart CA, Suzuki A, Rhein RK, Pollock TM, Levi CG. 2019. Oxidation behavior across composition space relevant to Co-based γ/γ' alloys. *Metall. Mater. Trans. A* 50:5445–58
84. Bunn JK, Fang RL, Albing MR, Mehta A, Kramer MJ, et al. 2015. A high-throughput investigation of Fe–Cr–Al as a novel high-temperature coating for nuclear cladding materials. *Nanotechnology* 26:274003
85. Payne MA, Miller JB, Gellman AJ. 2016. High-throughput screening across quaternary alloy composition space: oxidation of $(\mathrm{Al}_x\mathrm{Fe}_y\mathrm{Ni}_{1-x-y})_{\sim 0.8}\mathrm{Cr}_{\sim 0.2}$. *ACS Comb. Sci.* 18:559–68
86. Payne MA, Miller JB, Oliveros ME, Perez G, Gouvea CP, et al. 2016. Assessment of a high-throughput methodology for the study of alloy oxidation using $\mathrm{Al}_x\mathrm{Fe}_y\mathrm{Ni}_{1-x-y}$ composition gradient thin films. *ACS Comb. Sci.* 18:425–36
87. Metting CJ, Bunn JK, Underwood E, Smoak S, Hattrick-Simpers J. 2013. Combinatorial approach to turbine bond coat discovery. *ACS Comb. Sci.* 15:419–24
88. Payne MA, Miller JB, Gellman AJ. 2015. High-throughput characterization of early oxidation across $\mathrm{Al}_x\mathrm{Fe}_y\mathrm{Ni}_{1-x-y}$ composition space. *Corros. Sci.* 91:46–57
89. Wilke M, Teichert G, Gemma R, Pundt A, Kirchheim R, et al. 2011. Glow discharge optical emission spectroscopy for accurate and well resolved analysis of coatings and thin films. *Thin Solid Films* 520:1660–67
90. Muster TH, Trinchi A, Markley TA, Lau D, Martin P, et al. 2011. A review of high throughput and combinatorial electrochemistry. *Electrochim. Acta* 56:9679–99
91. Taylor SR. 2011. The investigation of corrosion phenomena with high throughput methods: a review. *Corros. Rev.* 29:135–51
92. Whitfield MJ, Bono D, Wei L, Van Vliet KJ. 2014. High-throughput corrosion quantification in varied microenvironments. *Corros. Sci.* 88:481–86
93. White PA, Smith GB, Harvey TG, Corrigan PA, Glenn MA, et al. 2012. A new high-throughput method for corrosion testing. *Corros. Sci.* 58:327–31
94. Liu J, Liu N, Sun M, Li J, Sohn S, Schroers J. 2019. Fast screening of corrosion trends in metallic glasses. *ACS Comb. Sci.* 21:666–74
95. Jargelius-Pettersson RFA. 1998. Application of the pitting resistance equivalent concept to some highly alloyed austenitic stainless steels. *Corrosion* 54:162–68
96. Taylor CD, Lu P, Saal J, Frankel GS, Scully JR. 2018. Integrated computational materials engineering of corrosion resistant alloys. *NPJ Mater. Degrad.* 2:6
97. Chang Y-J, Jui C-Y, Lee W-J, Yeh A-C. 2019. Prediction of the composition and hardness of high-entropy alloys by machine learning. *JOM* 71:3433–42
98. Coury FG, Wilson P, Clarke KD, Kaufman MJ, Clarke AJ. 2019. High-throughput solid solution strengthening characterization in high entropy alloys. *Acta Mater.* 167:1–11
99. Hemker KJ, Sharpe WN. 2007. Microscale characterization of mechanical properties. *Annu. Rev. Mater. Res.* 37:93–126
100. Gianola DS, Eberl C. 2009. Micro- and nanoscale tensile testing of materials. *JOM* 61:24
101. Dobi D, Junghans E. 1999. Determination of the tensile properties of specimens with small dimensions. *KZLTET* 33:451–57
102. Shade PA, Kim S-L, Wheeler R, Uchic MD. 2012. Stencil mask methodology for the parallelized production of microscale mechanical test samples. *Rev. Sci. Instrum.* 83:053903
103. Heckman NM, Ivanoff TA, Roach AM, Jared BH, Tung DJ, et al. 2020. Automated high-throughput tensile testing reveals stochastic process parameter sensitivity. *Mat. Sci. Eng. A* 772:138632
104. Miracle DB, Majumdar B, Wertz K, Gorsse S. 2017. New strategies and tests to accelerate discovery and development of multi-principal element structural alloys. *Scr. Mater.* 127:195–200
105. García TE, Rodríguez C, Belzunce FJ, Suárez C. 2014. Estimation of the mechanical properties of metallic materials by means of the small punch test. *J. Alloys Cmpds.* 582:708–17
106. Leclerc N, Khosravani A, Hashemi S, Miracle DB, Kalidindia SR. 2021. Correlation of measured load-displacement curves in small punch tests with tensile stress-strain curves. *Acta Mater.* 204:116501
107. Hornbuckle BC, Murdoch HA, Roberts AJ, Kecskes LJ, Tschopp MA, et al. 2017. Property mapping of friction stir welded Al-2139 T8 plate using site specific shear punch testing. *Mat. Sci. Eng. A* 682:192–201

108. Springer H, Raabe D. 2012. Rapid alloy prototyping: compositional and thermo-mechanical high throughput bulk combinatorial design of structural materials based on the example of 30Mn–1.2C–xAl triplex steels. *Acta Mater*. 60:4950–59
109. Kirklin S, Saal JE, Hegde VI, Wolverton C. 2016. High-throughput computational search for strengthening precipitates in alloys. *Acta Mater*. 102:125–35
110. Nyshadham C, Oses C, Hansen JE, Takeuchi I, Curtarolo S, Hart GLW. 2017. A computational high-throughput search for new ternary superalloys. *Acta Mater*. 122:438–47
111. Labusch R. 1970. A statistical theory of solid solution hardening. *Phys. Status Solidi B* 41:659–69
112. Toda-Caraballo I. 2017. A general formulation for solid solution hardening effect in multicomponent alloys. *Scr. Mater.* 127:113–17
113. Toda-Caraballo I, Rivera-Díaz-del-Castillo PEJ. 2015. Modelling solid solution hardening in high entropy alloys. *Acta Mater*. 85:14–23
114. Menou E, Tancret F, Toda-Caraballo I, Ramstein G, Castany P, et al. 2018. Computational design of light and strong high entropy alloys (HEA): obtainment of an extremely high specific solid solution hardening. *Scr. Mater.* 156:120–23
115. Rao SI, Antillon E, Woodward C, Akdim B, Parthasarathy TA, Senkov ON. 2019. Solution hardening in body-centered cubic quaternary alloys interpreted using Suzuki's kink-solute interaction model. *Scr. Mater.* 165:103–6
116. Tu P, Zheng Y, Zhuang C, Zeng X, Zhu H. 2019. A high-throughput computation framework for generalized stacking fault energies of pure metals. *Comput. Mater. Sci.* 159:357–64
117. Kivy MB, Zaeem MA. 2017. Generalized stacking fault energies, ductilities, and twinnabilities of CoCrFeNi-based face-centered cubic high entropy alloys. *Scr. Mater*. 139:83–6
118. Jalali SIA, Kumar P, Jayaram V. 2020. Microstructural equivalence between bending and uniaxial creep. *Scr. Mater.* 186:99–103
119. Jalali SIA, Kumar P, Jayaram V. 2020. Customized high-temperature bending with DIC for high-throughput determination of creep parameters: technique, instrumentation, and optimization. *JOM* 72:4522–38
120. Jalali SIA, Jayaram V, Kumar P. 2021. Creep micromechanics in meso-length scale samples. *Acta Mater*. 205:116535
121. Dobeš F, Milička K. 2009. Application of creep small punch testing in assessment of creep lifetime. *Mat. Sci. Eng. A* 510–511:440–43
122. Lee J, Wall JJ, Rogers JR, Rathz TJ, Choo H, et al. 2014. Non-contact measurements of creep properties of niobium at 1985°C. *Meas. Sci. Technol*. 26:015901
123. Alegre JM, Cuesta II, Barbachano HL. 2015. Determination of the fracture properties of metallic materials using pre-cracked small punch tests. *Fatigue Fract. Eng. Mater. Struct.* 38:104–12
124. Venkatraman K, Jayaram V. 2020. Crack velocity measurements through continuous stiffness monitoring of cyclically loaded notched micro-beams of thin graded Pt–Ni-Al bond coats. *Int. J. Fract*. 227:15–37
125. ASTM Int. 2010. *Standard Test Methods for Determining Hardenability of Steel, ASTM A255–10*. West Conshohocken, PA: ASTM Int. **http://www.astm.org/Standards/A255.htm**
126. Semiatin SL. 2004. Evolution of microstructure during hot working. In *Handbook of Workability and Process Design*, ed. GE Dieter, HA Kuhn, SL Semiatin, pp. 35–44. Materials Park, OH: ASM Int.
127. Miracle DB, Miller JD, Senkov ON, Woodward C, Uchic MD, Tiley J. 2014. Exploration and development of high entropy alloys for structural applications. *Entropy* 16:494–525
128. Zambaldi C, Yang Y, Bieler TR, Raabe D. 2012. Orientation informed nanoindentation of α-titanium: indentation pileup in hexagonal metals deforming by prismatic slip. *J. Mater. Res.* 27:356–67
129. Chakraborty A, Eisenlohr P. 2017. Evaluation of an inverse methodology for estimating constitutive parameters in face-centered cubic materials from single crystal indentations. *Eur. J. Mech. A Solids* 66:114–24
130. Chakraborty A, Zhang C, Balachandran S, Bieler TR, Eisenlohr P. 2020. Assessment of surface and bulk-dominated methodologies to measure critical resolved shear stresses in hexagonal materials. *Acta Mater*. 184:241–53
131. Li Z, Ludwig A, Savan A, Springer H, Raabe D. 2018. Combinatorial metallurgical synthesis and processing of high-entropy alloys. *J. Mater. Res.* 33:3156–69

132. Zhao JC. 2001. A combinatorial approach for efficient mapping of phase diagrams and properties. *J. Mater. Res.* 16:1565–78
133. Zhao JC. 2001. A combinatorial approach for structural materials. *Adv. Eng. Mat.* 3:143–47
134. Campbell CE, Boettinger WJ, Kattner UR. 2002. Development of a diffusion mobility database for Ni-base superalloys. *Acta Mater*. 50:775–92
135. Campbell CE, Zhao JC, Henry MF. 2004. Comparison of experimental and simulated multicomponent Ni-base superalloy diffusion couples. *J. Phase Equilib. Diffus.* 25:6–15
136. Zhao JC, Jackson MR, Peluso LA, Brewer LN. 2002. A diffusion-multiple approach for mapping phase diagrams, hardness, and elastic modulus. *JOM* 54:42–45
137. Lewandowski JJ, Seifi M. 2016. Metal additive manufacturing: a review of mechanical properties. *Annu. Rev. Mater. Res.* 46:151–86
138. Joseph J, Imran M, Hodgson PD, Barnett MR, Fabijanic DM. 2020. Towards the large-scale production and strength prediction of near-eutectic $Al_xCoCrFeNi_{2.1}$ alloys by additive manufacturing. *Manuf. Lett.* 25:16–20
139. Luo S, Zhao C, Su Y, Liu Q, Wang Z. 2020. Selective laser melting of dual phase $AlCrCuFeNi_x$ high entropy alloys: formability, heterogeneous microstructures and deformation mechanisms. *Addit. Manuf.* 31:100925
140. Dippo OF, Kaufmann KR, Vecchio KS. 2021. High-throughput rapid experimental alloy development (HT-READ). arXiv:2102.06180 [cond-mat.mtrl-sci]
141. Sistla HR, Newkirk JW, Liou FF. 2015. Effect of Al/Ni ratio, heat treatment on phase transformations and microstructure of $Al_xFeCoCrNi_{2-x}$ ($x = 0.3$, 1) high entropy alloys. *Mater. Des.* 81:113–21
142. Xiang S, Luan H, Wu J, Yao KF, Li J, et al. 2019. Microstructures and mechanical properties of CrMnFeCoNi high entropy alloys fabricated using laser metal deposition technique. *J. Alloys Cmpds.* 773:387–92
143. Dowling L, Kennedy J, O'Shaughnessy S, Trimble D. 2020. A review of critical repeatability and reproducibility issues in powder bed fusion. *Mater. Des.* 186:108346
144. Senkov ON, Miller JD, Miracle DB, Woodward C. 2015. Accelerated exploration of multi-principal element alloys for structural applications. *Calphad* 50:32–48
145. Boyce BL, Uchic MD. 2019. Progress toward autonomous experimental systems for alloy development. *MRS Bull*. 44:273–80
146. Nikolaev P, Hooper D, Webber F, Rao R, Decker K, et al. 2016. Autonomy in materials research: a case study in carbon nanotube growth. *NPJ Comput. Mater.* 2:16031
147. Gongora AE, Xu B, Perry W, Okoye C, Riley P, et al. 2020. A Bayesian experimental autonomous researcher for mechanical design. *Sci. Adv.* 6:eaaz1708
148. Maruyama B. 2017. Scientists pick AI for lab partner. *SIGNAL Magazine*, Sept. 1. **https://www.afcea.org/content/scientists-pick-ai-lab-partner**
149. Sahoo KC, Goyal S, Ganesan V, Vanaja J, Reddy GV, et al. 2019. Analysis of creep deformation and damage behaviour of 304HCu austenitic stainless steel. *Mater. High Temp.* 36:388–403